Received: 22 June 2021 | Revised: 24 January 2022 | Accepted: 29 January 2022

DOI: 10.1002/hipo.23408

RESEARCH ARTICLE

WILEY

Interneuron diversity in the rat dentate gyrus: An unbiased in vitro classification

Claudius E. Degro[1] | Felix Bolduan[1] | Imre Vida[1] | Sam A. Booker[1,2,3]

[1]Institute for Integrative Neuroanatomy, Charité - Universitätmedizin Berlin, Berlin, Germany

[2]Centre for Discovery Brain Sciences, University of Edinburgh, Edinburgh, UK

[3]Simons Initiative for the Developing Brain, University of Edinburgh, Edinburgh, UK

Correspondence
Imre Vida, Institute for Integrative Neuroanatomy, Charité - Universitätmedizin Berlin, Berlin, Germany.
Email: imre.vida@charite.de

Sam A. Booker, Centre for Discovery Brain Sciences, University of Edinburgh, Edinburgh, UK.
Email: sbooker@ed.ac.uk

Funding information
Deutsche Forschungsgemeinschaft, Grant/Award Numbers: EXC 257, FOR 2143; Simons Initiative for the Developing Brain

[Correction added on March 01, 2022, after first online publication: word supervised has been changed to unsupervised in the abstract.]

Abstract

Information processing in cortical circuits, including the hippocampus, relies on the dynamic control of neuronal activity by GABAergic interneurons (INs). INs form a heterogenous population with defined types displaying distinct morphological, molecular, and physiological characteristics. In the major input region of the hippocampus, the dentate gyrus (DG), a number of IN types have been described which provide synaptic inhibition to distinct compartments of excitatory principal cells (PrCs) and other INs. In this study, we perform an unbiased classification of GABAergic INs in the DG by combining in vitro whole-cell patch-clamp recordings, intracellular labeling, morphological analysis, and unsupervised cluster analysis to better define IN type diversity in this region. This analysis reveals that DG INs divide into at least 13 distinct morpho-physiological types which reflect the complexity of the local IN network and serve as a basis for further network analyses.

KEYWORDS
cluster analysis, dentate gyrus, GABA, inhibition, interneuron, neuron diversity

1 | INTRODUCTION

Neuronal activity in cortical circuits requires a tightly controlled and dynamic balance of excitatory and inhibitory synaptic neurotransmission. This balance emerges from, and is maintained by, local circuit interactions of excitatory glutamatergic PrCs and inhibitory GABAergic INs (Booker & Vida, 2018; Freund & Buzsáki, 1996; Pelkey et al., 2017). In contrast to the mostly homogenous populations of PrCs, INs are highly diverse with respect to their morpho-physiological characteristics. As such, distinct IN types are presumed to play divergent roles in the neural circuitry (Bartos et al., 2007; Mott et al., 1997; Somogyi & Klausberger, 2005; Vida et al., 2006). This functional diversity of INs is particularly important in their control of PrC excitability by feed-forward and feedback inhibition, leading to temporal coordination of ensemble activity and network oscillations required for integration of synaptic information (Buzsáki, 1984; Gloveli et al., 2005).

In mammals, the hippocampal formation encodes egocentric spatial and contextual information and acts as an integrator for multimodal streams leading to memory trace formation (Andersen et al., 1973; Morris et al., 1982; O'Keefe & Dostrovsky, 1971). Spatial information arrives at the hippocampus from the entorhinal cortex (EC) through the dentate gyrus (DG), which transforms the dense firing pattern of the EC into a sparse output for the downstream *Cornu Ammonis* (first CA3 and then CA1 area; Hainmueller & Bartos, 2020). This sparsification and orthogonalization of cortical code in the DG depends heavily on the activity of diverse INs innervating the two major PrC types, dentate granule cells (DGCs) and hilar mossy cells (MCs; Amaral et al., 2007). While previous studies have described several distinct IN types in the rat DG (Armstrong et al., 2012; Ceranik

et al., 1997; Han et al., 1993; Mott et al., 1997; Seress & Ribak, 1983; Sik et al., 1997), a systematic and unbiased analysis of their diversity has not been performed.

Prior studies on DG INs have considered their morphology as a primary classifier. Their physiological diversity has been almost solely defined by their action potential (AP) discharge properties, subdividing INs into fast-, regular-, or slow-spiking cells (Armstrong et al., 2011; Bartos et al., 2007; Gloveli et al., 2005; Sullivan et al., 2011; Vida et al., 2006; Ylinen et al., 1995). The first systematic analysis, integrating morphological and physiological properties to classify DG IN subtypes was performed in the mouse by Hosp et al., 2014 and revealed at least five IN classes. Previous estimates in the rat suggest a greater diversity (Booker & Vida, 2018), but a comprehensive determination of IN heterogeneity in the DG has yet to be performed.

Therefore, in the present study, we perform an unbiased, multivariate statistical approach to define DG IN diversity based on their morpho-physiological properties from in vitro brain tissue. Using a transgenic rat expressing the yellow fluorescent protein (YFP, Venus-variant) under the vesicular GABA transporter (vGAT) promoter (Uematsu et al., 2008), we targeted INs in a systematic and quasi-random manner for whole-cell patch-clamp recordings followed by morphological reconstruction and analysis. We then performed a *post hoc* cluster-analytical classification of IN types based on measured morpho-physiological characteristics. Our results revealed a higher IN diversity than previously reported, with IN types aligned to major synaptic pathways within the DG local circuit with implications for circuit function.

2 | MATERIALS AND METHODS

2.1 | Acute slice preparation

All experiments and animal procedures were performed in accordance with local (LaGeSo, Berlin, T 0215/11) and national guidelines (German Animal Welfare Act). To facilitate efficient and unbiased sampling, we used acute brain slices obtained from 18 to 26 day-old Wistar rats, expressing a modified YFP (Venus variant) in forebrain INs under the vGAT promoter (Uematsu et al., 2008).

In vitro hippocampal slices were prepared as previously described (Booker et al., 2014; Degro et al., 2015). Briefly, rats were anesthetized with isoflurane, decapitated, and the brains rapidly removed into ice-cold carbogenated (95% O_2/5% CO_2) sucrose-based artificial cerebrospinal fluid (sucrose-ACSF; in mM: 87 NaCl, 2.5 KCl, 25 $NaHCO_3$, 1.25 NaH_2PO_4, 25 Glucose, 75 Sucrose, 1 Na_2-Pyruvate, 1 Na_2-Ascorbate, 7 $MgCl_2$, 0.5 $CaCl_2$). Transverse hippocampal slices (300 μm nominal thickness) were cut from the ventromedial hippocampus on an oscillating blade vibratome (VT1200s, Leica, Germany) in ice-cold sucrose-ACSF. Slices were transferred to submerged storage chambers containing sucrose-ACSF warmed to 35°C for 30 min to allow for recovery. Slices were then stored at room temperature (20°C) in the same solution until recording.

2.2 | Whole-cell patch-clamp recordings

For electrophysiological recordings, slices were transferred to a submerged recording chamber and perfused with carbogenated, normal ACSF (in mM: 125 NaCl, 2.5 KCl, 25 $NaHCO_3$, 1.25 NaH_2PO_4, 25 Glucose, 1 Na_2-Pyruvate, 1 Na_2-Ascorbate, 1 $MgCl_2$, 2 $CaCl_2$). ACSF was flowed at a rate of 10–12 ml/min (Hájos et al., 2009) at a near physiological temperature (31-33°C) by an in-line heater (SuperTech, Switzerland). Slices were visualized using an upright microscope (BX-50, Olympus, Hamburg, Germany) equipped with a 40x water immersion objective lens (N.A. 0.8) and epifluorescent illumination. YFP-positive cells were selected for recordings from all layers of the DG (ML, molecular layer; GCL, granule cell layer; polymorphic layer, hilus). YFP-negative DGCs and MCs were recorded as reference populations from the GCL and the hilus, respectively. Recording pipettes were pulled from borosilicate glass capillaries (2 mm outer/1 mm inner diameter, Hilgenberg, Germany) on a horizontal pipette puller (P-97, Sutter Instruments, Novato, CA) and filled with intracellular solution (in mM: 130 K-gluconate, 10 KCl, 2 $MgCl_2$, 10 EGTA, 10 HEPES, 2 Na_2-ATP, 0.3 Na_2-GTP, 1 Na_2-Creatinine and 0.1% biocytin; 290–310 mOsm). The resistance of the filled pipettes was 3–5 MΩ. Whole-cell patch-clamp recordings were performed using a MultiClamp 700B amplifier (Molecular Devices, San Jose, CA) with all signals filtered online at 10 kHz using the built-in 4-pole Bessel filter (Axon Instruments, San Jose, CA), digitized and recorded at 20 kHz (NI USB-6212 BNC, National Instruments, Berkshire, UK) using WinWCP software (courtesy of John Dempster, Strathclyde University, Glasgow, UK). Data were analyzed offline using the open-source Stimfit software package (Guzman et al., 2014; http://www.stimfit.org).

2.3 | Measurement of intrinsic physiological properties

Physiological properties of neurons were analyzed in the whole-cell configuration. Resting membrane potential (V_m) was taken at baseline zero-current level in current-clamp mode at the start of the recordings and further physiological characterization was performed based on voltage responses to a family of hyper- to depolarizing current pulses ranging from −250 pA to 250 pA (in 50 pA steps, 500 ms duration) in a subset of neurons this was followed by a 500 pA pulse; liquid junction potential was not corrected. AP properties and threshold were analyzed based on the first AP at rheobase (average of the measured values from 3 traces), triggered by a series of small depolarizing current pulses applied to the V_m (10 pA increase, 500 ms duration). AP threshold was determined as the voltage where the rate-of-rise first exceeded 20 mV/ms. Fast and medium after-hyperpolarization (AHP) were defined as the first and second negative peaks in voltage following the AP measured from threshold. AP discharge frequency (APs overshooting 0 mV) was measured over the full 500 ms trace for depolarizing stimuli. AP adaptation was measured from a train of APs evoked at 250 pA and expressed as the ratio of the first and last interspike interval (ISI). Voltage sag was measured in response to −250 pA

current pulses as the difference between the peak and steady-state voltage response, expressed as percentage of peak (3-trace average). Membrane time-constant was calculated in current-clamp mode by fitting a mono-exponential function to the decay of the average response to small hyperpolarizing current pulses (−10 pA, 500 ms duration, 30-trace average). Finally, input resistance (R_{in}) and membrane capacitance (C_m) were assessed in voltage-clamp mode at −60 mV from the average response to small voltage steps (−10 mV, 500 ms duration, 10-trace average). R_{in} was calculated from the steady-state current at the end of the −10 mV pulse from the preceding baseline. C_m was derived by fitting a biexponential function to the decay of the capacitive current induced by the pulse following the equation:

$$C_m = \tau(w) \times (1/R_s + 1/R_{in})$$

where $\tau(w)$ is the weighted time-constant and R_s the series resistance. A detailed overview and description of all assessed physiological parameters are given in Table S1.

2.4 | Visualization, imaging, reconstruction, and morphological analysis

Morphological characterization of recorded neurons was performed as previously described (Degro et al., 2015). Briefly, following completion of recording, an outside-out patch configuration was obtained and slices were fixed immediately with 4% paraformaldehyde (PFA) in 0.1 M phosphate buffer (PB) overnight at 4°C. Slices were then rinsed repeatedly in PB prior to incubation with Alexa Fluor 647-conjugated streptavidin (1:1000, Invitrogen, Dunfermline, UK), diluted in PB containing 0.1% Triton X-100 and 0.05% sodium azide (NaN_3), overnight at 4°C. Slices were mounted on glass slides, containing a 300 μm thick agar spacer, with a polymerizing mounting medium (Fluoromount-G, Southern Biotech, Birmingham, AL) and cover-slipped.

All recorded cells were imaged on a laser scanning confocal microscope (FluoView 1000, Olympus) with either ×20 (NA 0.75) or oil-immersion ×60 (NA 1.3) objective lenses. For 3D reconstructions of the imaged cells, image stacks were collected along the *z*-axis of the cells (0.5 or 1 μm steps, 4 μs pixel dwell time, 1024 × 1024 or 2048 × 2048 resolution). Neighboring z-series images were then stitched using the FIJI software package (http://fiji.org) and reconstructions of the labeled neurons were made with the semi-automatic Simple Neurite Tracer plug-in for FIJI (Longair et al., 2011). Traces of the neuronal structure were then reformatted in '.swc' files for post hoc corrections: *z*-axis slice shrinkage was compensated by calculating and applying a correction factor representing the quotient of the original slice thickness (300 μm) and the imaged thickness of the specimen. Segmented neuronal reconstructions were then smoothed in NEURON (Hines & Carnevale, 1997) using a Gaussian spatial filter (three-point window, single run in the *x*/*y*-plane, and 10 iterations for values along the *z*-axis; customized hoc script, Bolduan et al., 2020) to reduce imaging artifacts. Finally, morphometric parameters were analyzed with (1) the open-source L-measure software package (Scorcioni et al., 2008; branch order, branch pathlength, bifurcation angle, no. of dendritic stems), (2) R macroinstructions (Ripley, 2001; The R Project for Statistical Computing; https://www.r-project.org; customized R scripts: axon density parameters), and (3) the NEURON simulation program (Hines & Carnevale, 1997; customized hoc scripts: axon and dendritic polarity). Sholl analysis parameters and compartment-specific distribution of the axonal and dendritic arbor were assessed in FIJI by using the Sholl Analysis plug-in and the Segmentation Editor plug-in, respectively. Then calculating the relative length axon or dendrite within a given region of interest (ROI). A detailed overview and description of all assessed morphological parameters are given in Table S2.

2.5 | Immunohistochemistry

To reveal differences in neurochemical marker expression of recorded neurons, we performed immunofluorescent labeling. Slices were first rinsed in 25 mM PB containing 0.9% NaCl (PBS) and then blocked in a solution containing 10% Normal Goat Serum, 0.3% or 1% Triton X-100, and 0.05% NaN_3, diluted in PBS, for 60 min at room temperature. Slices were then transferred to a mixture of primary antibodies (PBS containing 5% Normal Goat Serum, 0.3% Triton X-100, and 0.05% NaN_3) for 120 min (room temperature) before washing in PBS and subsequently incubated in a secondary antibody solution (Alexa Fluor 405/546 or 594, 1:1000, Invitrogen, diluted in PBS containing 3% Normal Goat Serum, 0.1% Triton X-100 and 0.05% NaN_3, overnight, 4°C). Finally, slices were rinsed in PBS, desalted with PB, and mounted on glass slides. The presence of immunofluorescence was tested by confocal imaging over the soma and proximal dendrites.

Selection of the different primary antibodies was based on previously described neurochemical distributions in the DG (Freund & Buzsáki, 1996; Hosp et al., 2014) and is shown in Table 1. When possible, neurons were assessed for 2–3 neurochemical markers simultaneously.

2.6 | Kernel principal component and cluster analysis

Morpho-physiological cluster analysis was performed with a total of 87 fully reconstructed neurons (80 INs, 4 DGCs, and 3 MCs) based on 53 parameters (38 morphological and 15 physiological). A Kaiser–Meyer–Olkin (KMO) index of 0.53 and a significant Bartlett's test of sphericity ($p < .001$) indicated factorization sampling adequacy of the combined morpho-physiological data (morphological dataset: KMO index: 0.52, Bartlett's test of sphericity: $p < .001$; physiological dataset: KMO index: 0.62, Bartlett's test of sphericity: $p < .001$; Bartlett, 1950, Table S12) using a KMO index cut-off >0.5 (Field, 2000; Kaiser, 1974). In view of the nonlinear structure of the given dataset, a Kernel principal component analysis (KPCA; Karatzoglou et al., 2004; Schölkopf et al., 1998) was then applied prior to cluster analysis. KPCA was performed, based on normalized parameters, by calculating a kernel matrix using the following radial basis function (RBF) kernel

TABLE 1 Summary of primary antibodies

Neuropeptide	Host species	Manufacturer	Dilution
Calbindin (CB)	Mouse monoclonal	SWANT, Marly, Switzerland	1:2000
Calretinin (CR)	Rabbit polyclonal	SWANT, Marly, Switzerland	1:4000
Cholecystokinin (CCK)	Mouse monoclonal	G. Ohning, CURE, UCLA, USA	1:5000
Pro-cholecystokinin (pCCK)	Rabbit polyclonal	Frontiers Institute, Japan	1:1000
Neuronal nitric oxide synthase (nNOS)	Mouse monoclonal	Invitrogen, Carlsbad, CA, USA	1:300
Neuropeptide Y (NPY)	Rabbit polyclonal	Peninsula Laboratories, USA	1:2000
Parvalbumin (PV)	Mouse monoclonal	SWANT, Marly, Switzerland	1:5000
Somatostatin (SST)	Rabbit polyclonal	Peninsula Laboratories, USA	1:2000

Note: Primary antibodies used for immunohistological labeling in this study, including host species, source, and dilution used.

$$k(x,x') = \exp\left(-\sigma \|x - x'\|^2\right)$$

followed by a centering of the kernel matrix and principal component calculation ("kpca" function, kernlab package, R). The inverse kernel width, σ, for the RBF kernel was calculated using the "sigest" function (kernlab package, R) and set to the 0.5 quantile value. The scree-test (defined as $k - 1$) was then used to select the principal components to retain (k is defined as the kink-point in a principal component/eigenvalue plot; Bacher et al., 2010; Cattell, 1966). Finally, data were projected onto the extracted principal components, from which a deterministic hierarchical–agglomerative cluster analysis, following Ward's minimum variance method (HCA Ward) was performed ("hclust" function, stats package, R). As such, the proximity measure that describes the distance between 2 clusters equated to the squared Euclidean distance (Tables S9–S11). The cluster results were represented by a classic dendrogram, with the optimal number of clusters calculated using the inverse scree-plot where the number of clusters to retain equals k, when k is the kink-point in a total number of clusters/merging level plot ("elbow-criterion", Bacher et al., 2010). Cluster analyses of morphological and physiological characteristics alone were performed identically to the above-described algorithm. Additional clustering methods (k-means and divisive analysis, DIANA) that are reported in the Supporting Information were performed using the "kmeans" function (stats package, R) and the "diana" function (cluster package, R). Full details of all R functions used are outlined in the Supporting Information.

2.7 | Chemicals and pharmacological tools

All chemicals were obtained from either Sigma Aldrich (Munich, Germany) or Carl Roth (Karlsruhe, Germany). Biocytin was obtained from Life Technologies (Dunfermline, UK). Working solutions (ACSF) were prepared fresh on each experimental day.

2.8 | Statistical analysis

Statistics were performed with R (Ripley, 2001; The R Project for Statistical Computing; https://www.r-project.org) and plots of data were generated with R and GraphPad Prism 9.0.0 (GraphPad Software, San Jose, CA). Statistical significance was assumed if the resulting p-value was <.05. This was assessed using either a two-way ANOVA combined with Tukey´s test or a Kruskal–Wallis test. Data are shown as mean ± SD throughout.

3 | RESULTS

3.1 | Identification of INs and PrCs in the DG

To investigate the diversity of DG INs, we performed whole-cell patch-clamp recordings combined with intracellular biocytin labeling in acute hippocampal slices from vGAT-YFP rats (Uematsu et al., 2008). These rats expressed YFP under the vGAT promoter that enabled an efficient and systematic sampling of INs. In slices from these rats, YFP-positive neurons were scattered in all layers of the DG, with the highest abundance found in the polymorphic hilus region adjacent to the GCL (Figure 1a).

Recorded INs displayed a variety of heterogeneous electrophysiological properties, ranging from high-frequency, non-accommodating to regular-spiking, accommodating AP discharge patterns (Figure 1b–d, insets). Visualization of intracellularly labeled cells also revealed divergent morphologies with respect to dendrite and axon distributions (Figure 1b–d). Depending on soma localization, the dendrites of these INs displayed horizontal, vertical, pyramidal-like, or multipolar morphologies, which were typically non-spiny or occasionally sparsely spiny. The axon of INs typically emerged from the soma or a proximal dendrite forming a dense local axon. This axon often showed a laminar distribution—consistent with a compartment-specific synaptic output within the DG. Visual inspection of the INs suggested that this sample included cells with previously described morpho-physiological properties: for example, perisomatic inhibitory fast-spiking basket cells (BC, Figure 1b) and dendrite-targeting INs, such as hilar perforant pathway associated (HIPP) cells (Figure 1c). *Post hoc* immunolabeling for neurochemical IN markers demonstrated the differential presence of parvalbumin (PV) and somatostatin (SST) in these INs, respectively, consistent with their putative identity (Figure 1b,c, insets). However, in contrast to the previously described types, many INs displayed divergent morpho-physiological properties with varied neurochemical

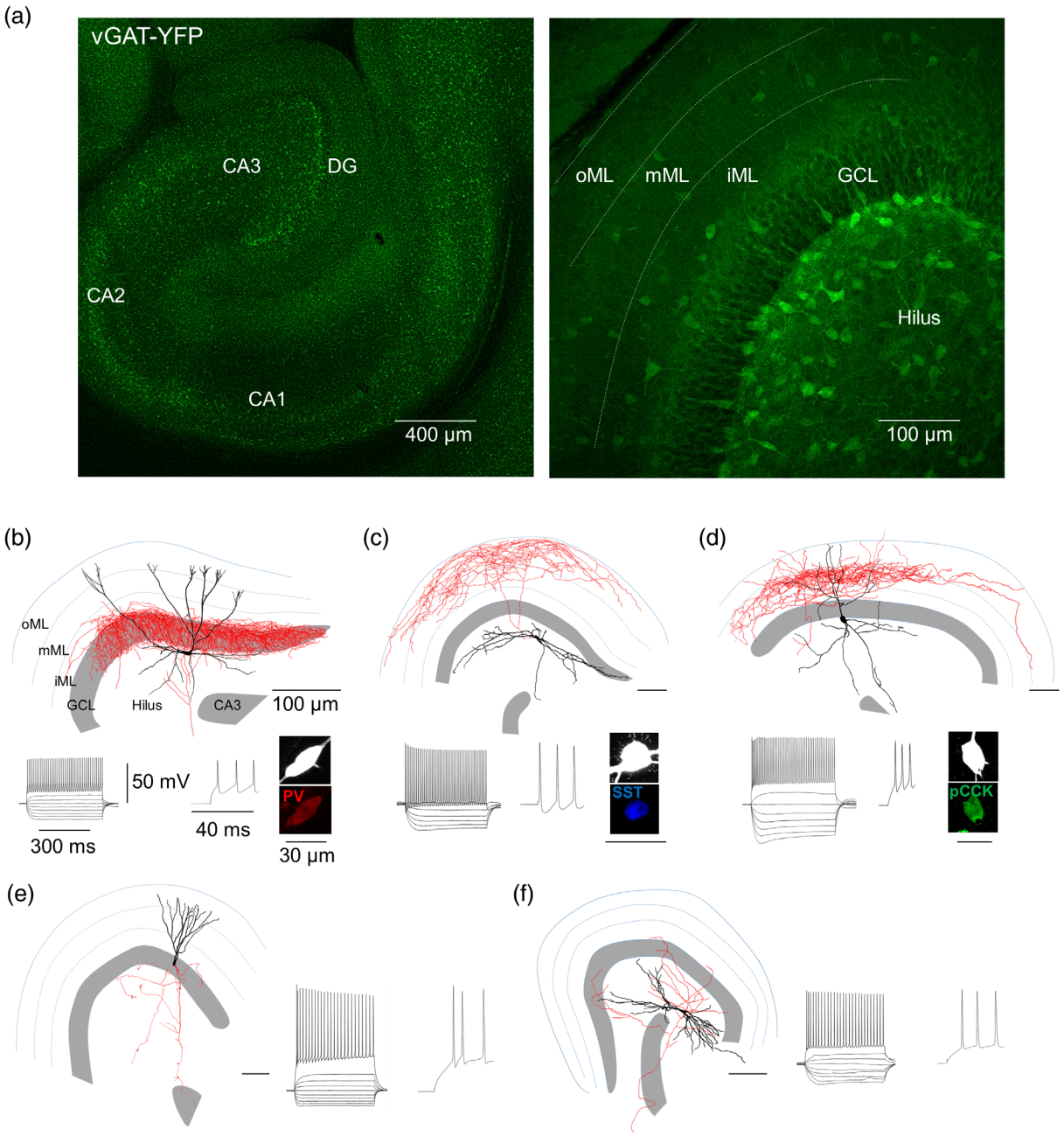

FIGURE 1 VGAT-YFP expression and cell types of the DG. (a) Overview of the hippocampal formation (×4 and ×20 magnification) taken from 300 µm thick transverse hippocampal slices of vGAT-YFP rats. YFP-positive neurons can be found in all layers with an abundance at the hilus-GCL border. YFP-negative neurons are found densely packed in the GCL and scattered over the hilus. (b–d) reconstructions of YFP-positive neurons: a BC (b), a HIPP cell (c), and an unknown cell type (d). (e,f) reconstructions of YFP-negative neurons: a DGC in the GCL (e) and a MC from the hilus (f). (b–f) Soma and dendrites are shown in black and the axon in red. Insets illustrate voltage responses to a set of hyper- to depolarizing current pulses (−250 pA to 500 pA, 50 pA steps, 500 ms duration) (left) and an enlarged detail of the action potential discharge at 500 pA (middle). Insets (right), immunopositivity for PV (b), SST (c), and pCCK (d) in the biocytin filled cells. BC, basket cell; Bio, biocytin; CA, cornu ammonis; DG, dentate gyrus; DGC, dentate granule cell; GCL, granule cell layer; HIPP, hilar perforant pathway associated cell; iML, inner molecular layer; MC, mossy cell; mML, middle molecular layer; oML, outer molecular layer; pCCK, pro-cholecystokinin; PV, parvalbumin; SST, somatostatin; vGAT, vesicular GABA transporter; YFP, yellow fluorescent protein

marker expression such as pro-cholecystokinin (pCCK, Figure 1d), indicating that the previous classification of DG INs is likely incomplete.

YFP-negative neurons formed two major populations: first with small, round somata, densely packed in the GCL, and second with large somata localized to the hilus. Recordings from YFP-negative cells located in the GCL displayed electrophysiological characteristics of DGCs including accommodating discharge patterns and hyperpolarized membrane potentials. Visualization revealed typical DGC morphology consisting of 3–6 monopolar, densely spiny dendrites that fanned out into the ML covering all sublayers. DGC axons uniformly emerged from

the opposite pole of the soma and projected through the hilus and toward the CA3 (Figure 1e). Recordings from YFP-negative neurons in the hilus showed morpho-physiological features consistent with MCs, including a bipolar somatodendritic domain confined to the hilus, densely covered with simple and large complex spines. MCs axonal projections were restricted to the hilus and the inner ML (iML, Figure 1f).

To define the diversity of DG INs in an unbiased manner, we next performed a detailed morphological and electrophysiological analysis of the recorded neurons combined with an unbiased hierarchical clustering. We performed this analysis with complete morphological and electrophysiological characterization on a total of 80 YFP-positive INs and 7 YFP-negative PrCs.

3.2 | Cluster analysis of DG IN morphotypes

A major criterion in previous classifications of IN and PrC types was their morphology, in particular the laminar distribution of axon and dendrites (Booker & Vida, 2018; Freund & Buzsáki, 1996; Han et al., 1993; Pelkey et al., 2017). As such, we first performed a hierarchical cluster analysis of morphological parameters using Ward's minimum variance method (Figure 2). All neurons were three-dimensionally reconstructed, from which 38 morphological parameters were derived (axon: 20, dendrites: 16, soma: 2, Table S2). Based on these parameters, we first performed a KPCA to achieve a general dimensional reduction. By applying the scree-test (Cattell, 1966), we

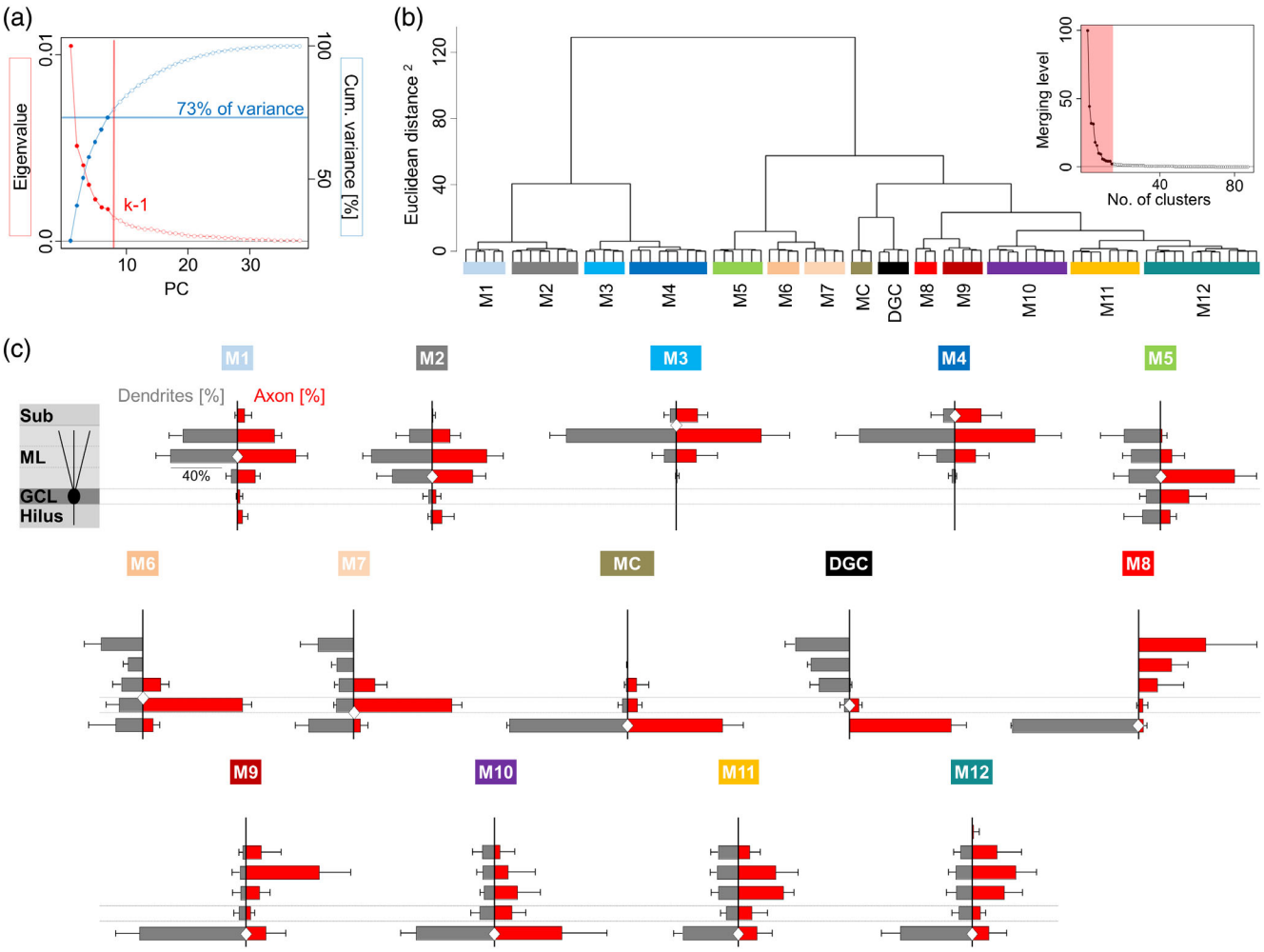

FIGURE 2 Hierarchical cluster analysis of DG INs based on their morphological characteristics. (a) Eigenvalue/cumulative variance plot of the extracted principal components. Principal components that were retained for clustering ($N = 7$, *scree-test*, $k - 1$) are illustrated as red and blue circles together with the kink-point of the eigenvalue graph (k, red vertical line) and the contributed cumulative variance (blue horizontal line). (b) Dendrogram of the morphological cluster analysis obtained using Ward's minimum variance method. The 14 different clusters identified are illustrated by different colors (M1–M12, MC, DGC). M1: $N = 5$, M2: $N = 8$, M3: $N = 5$, M4: $N = 9$, M5: $N = 6$, M6: $N = 4$, M7: $N = 5$, MC: $N = 3$, DGC: $N = 4$, M8: $N = 3$, M9: $N = 5$, M10: $N = 9$, M11: $N = 8$, M12: $N = 13$. Inset represents the inverse scree plot (no. of clusters/merging level) to define the optimal number of clusters that were maintained (pale red area) based on the inflection point of the graph (*elbow-criterion*). (c) Summary bar charts of the layer-specific axonal (red) and dendritic (gray) distribution (as proportion of the total length, %, mean ± SD) of each cluster aligned to the inset scheme (left). Soma localization is indicated as a white diamond on the *y*-axis. The molecular layer (ML) is subdivided into inner, middle, and outer ML (gray dashed lines). DGC, dentate granule cell; GCL, granule cell layer; MC, mossy cell; PC, principal component; Sub, subiculum

included the first seven principal components in our HCA Ward which together contributed 73% of the morphological variance (Figure 2a).

To determine the number of neuronal clusters, we next applied the "elbow"-criterion (Bacher et al., 2010; Figure 2b, inset) and identified 14 distinct morphological clusters, 12 of which comprised different YFP-positive IN morphotypes. The two main branches of the dendrogram generally comprised INs with soma localization either restricted to the ML or the hilus/GCL, associated with the largest squared Euclidean distance (Figure 2b). The first branch comprised ML INs that formed 4 of the 12 clusters (M1–M4). The second branch included five clusters of INs preferentially localized to the hilus (M8–M12) and three clusters with somata within, or adjacent to the GCL (M5–M7). The individual clusters in both branches showed further divergence with respect to their axonal and dendritic distributions (Figure 2b,c). Indeed, in the ML IN clusters, we observed both previously described and novel morphotypes. While most clusters with somata in the ML displayed prominent axon alignment within this layer, differences existed in the pattern of branching and the precise laminar distribution of these collaterals. Notably, M3 neurons ($N = 5$) had a highly branched, dense, focal axon and dendrites largely restricted to the outer ML (oML), comparable to those of neurogliaform cells (NGFCs), but also projected into the subiculum/CA1. By contrast, M2 cells ($N = 8$) had somata and dendrites confined to the ML and an axon which showed a broad horizontal distribution in the middle ML (mML) and to a lesser extent in the oML and iML, characteristics reminiscent of ML perforant pathway associated (MOPP) neurons.

In addition, we identified three clusters of ML morphotypes which were not previously described: M1 cells ($N = 5$) revealed an axonal distribution comparable to that of the MOPP like (M2) cluster, but that also projected across the hippocampal fissure into the subiculum/CA1. In contrast to M2 INs, their dendrites were mainly restricted to the mML and oML. M4 neurons ($N = 9$) were characterized by a somatodendritic localization in the oML direct adjacent to the hippocampal fissure and by a substantial axonal projection into the subiculum/CA1 (% of axon: 20.7 ± 15.7). Unlike NGFC like (M3) INs, M4 neurons displayed a larger horizontal extent of their axonal arbor with a reduced perisomatic axonal density (% of axon: 13.5 ± 3.7 vs. 25.6 ± 7.7, Table S3 and Figure S7). In contrast, the M5 cluster ($N = 6$) had somata and axons restricted to the iML, but with dendrites spanning all layers.

In the second branch of the dendrogram, we identified specific clusters that had morphologies resembling previously described IN types (Hosp et al., 2014). For example, the M6 ($N = 4$) and M7 ($N = 5$) clusters had somata localized in or adjacent to the GCL with dendrites spanning all layers. Their dense axonal arbors were largely confined to the GCL, corresponding to putative axo-axonic (AACs) and basket cells (BCs), respectively. The M8 cluster ($N = 3$) was characterized by neurons with spiny dendrites restricted to the hilus and axons localized to the outer two-thirds of the ML, bearing a strong resemblance to hilar perforant pathway associated (HIPP) cells. M10 neurons ($N = 9$) showed a preferential axonal projection to the iML, a characteristic similar to hilar commissural–associational pathway associated (HICAP) cells. However, in contrast to the original description of HICAP neurons, the majority of the M10 axon collaterals were in the hilus. M11 cells ($N = 8$) featured an axonal arbor that covered all layers of the ML, consistent with total molecular layer (TML) cells. In addition to these previously described hilar IN morphotypes, we identified two IN clusters within this group that had markedly different morphologies. Specifically, M12 ($N = 13$) had a dendritic distribution covering all layers of the DG, but possessed an axon that preferentially ramified in the mML (Figure 2c). M9 ($N = 5$) displayed a dendritic domain restricted to the hilus, but had an axon that appeared bistratified, targeting both the outer two-thirds of the ML and the hilus.

Importantly, YFP-negative PrCs, included in the analysis for reference, clearly segregated from the above IN clusters, with both DGCs and MCs clustering into two distinct morphotypes (Figure 2b). Comparison of the given HCA Ward with two different cluster methods (divisive hierarchical clustering, DIANA, and partitional clustering, k-means) generally showed a strong overlap of the revealed cluster constitutions, most distinct for the k-means clustering (89% overlap, Figure S4). A summary of the morphological dataset of each morphological cluster identified is presented in Figures S1 and S7 and in Tables S3 and S4.

3.3 | Cluster analysis of physiological properties of DG INs

INs show a variety of physiological properties (Scharfman, 1995) which have been previously used as a key dissector of types (Hosp et al., 2014), serving as a partial classifier for their wider diversity (Gouwens et al., 2020). As such, we next performed a cluster analysis based on the physiological properties of the recorded neurons (5 intrinsic membrane properties and 10 AP parameters, Table S1). After applying the scree-test on the KPCA results, we identified five principal components that contributed 81% of the observed variance (Figure 3a). These five principal components were retained and included in our HCA Ward, which resulted in a hierarchical classification subdividing the recorded neurons into eight physiological clusters (elbow-criterion) with distinct electrophysiological properties (P1–P8; Figure 3b,c). Comparison of the result obtained using Ward's minimum variance method with the other two clustering methods displayed a good correlation of the proposed cluster constitutions (k-means: 68% overlap; DIANA: 74% overlap; Figure S5), however, less pronounced than for morphological clustering.

Overall, the physiological clustering separated physiological (P)-types, including PrCs (P4 and P6) and INs (P1–3, P5, P7, and P8). This is reflected by diverse patterns of AP discharge from IN clusters and PrCs. Indeed, within the P-types, P1 ($N = 11$) represented typical fast-spiking INs, with small amplitude, rapid APs, and large and fast AHPs (Figure 4a, d,e). The remaining IN P-types had trains of APs with higher frequency discharge than PrCs, but displayed passive and active properties that were highly heterogeneous between clusters, thus reflecting cell-type-specific diversity (Figure 4b–e). A further key feature contributing to physiological clustering related to AP kinetics, as such we then compared these properties between P-types, both as the voltage response (Figure 4d) and as the first-derivative of the voltage (phase plots, Figure 4e). As expected from the diverse AP discharge patterns seen, the AP kinetics of P-types were distinct, with large-amplitude, fast APs in P4 ($N = 4$), corresponding to DGCs, and small-amplitude, fast APs in P1,

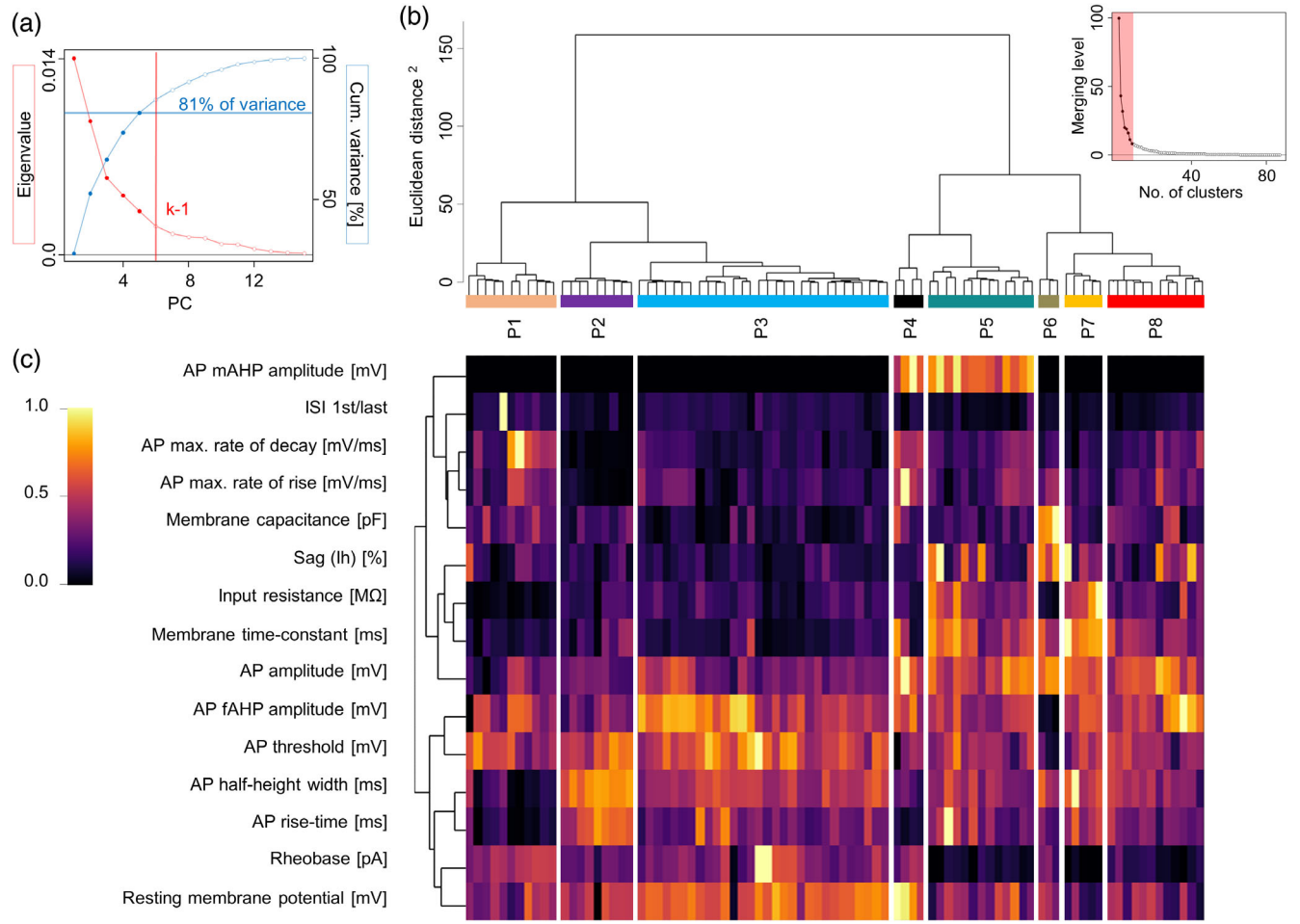

FIGURE 3 Hierarchical cluster analysis of DG INs based on their physiological characteristics. (a) Eigenvalue/cumulative variance plot of the extracted principal components. Principal components that were retained for clustering ($N = 5$, scree-test, $k - 1$) are illustrated as red and blue circles together with the kink-point of the eigenvalue graph (k, red vertical line) and the contributed cumulative variance (blue horizontal line) (b) Dendrogram of the physiological cluster analysis obtained using Ward's minimum variance method. The eight different clusters identified are illustrated by different colors (P1–P8). P1: $N = 11$, P2: $N = 9$, P3: $N = 30$, P4: $N = 4$, P5: $N = 13$, P6: $N = 3$, P7: $N = 5$, P8: $N = 12$. Inset represents the inverse scree plot (no. of clusters/merging level) to define the optimal number of clusters that were maintained (pale red area) based on the inflection point of the graph (elbow-criterion). (c) Heatmap of the normalized physiological parameters plotted for each neuron (columns). Physiological parameters are ordered based on an independent Ward clustering. AP, action potential; fAHP, fast after-hyperpolarization; ISI, interspike interval; mAHP, medium after-hyperpolarization; PC, principal component

corresponding to classic "fast-spiking" cells. The remaining INs and MCs displayed APs of similar amplitude, but with a spectrum of kinetic properties (Figure 4d,e). Based on previous observations (Hosp et al., 2014), the passive properties of DG INs are also divergent. To confirm this, we plotted the mean current–voltage relationship of each identified P-type in response to hyperpolarizing current pulses (Figure 4b). This agreed with both the spike discharge and AP kinetic properties, revealing a high degree of diversity in voltage response, ranging from low-resistance neurons (P1, P3, and P6) to those with much higher resistances (P5, P7, and P8; Figure 4b). In line with the P-type classification identiying distinct types of DG INs, phase-plots of APs revealed within cluster homogeneity of kinetics in some clusters (P2, P6–P7), while others displayed high variability (P1, P3–P5, and P8; Figure 4e). This was exemplified by several DGCs inappropriately being assigned to otherwise mostly IN clusters (P5), likely reflecting the more variable nature of electrophysiological recordings compared to anatomy alone.

This data shows that, while our physiological cluster analysis of DG neurons alone revealed that particular P-classes gave rise to distinct functional types, the total number of clusters identified based on electrical properties alone was lower than for the morphological classification and showed greater heterogeneity within type. A summary of the entire physiological dataset of each physiological cluster identified is presented in Figure S8 and in Tables S5 and S6.

3.4 | Correlation of morphological and physiological derived IN cluster

We next correlated the single-cell constitutions originated from the morphological and physiological parameter clustering to detect potential overlap and divergence between these two cluster results. Comparison of the separate cluster analyses (Figure 4f) showed that while some

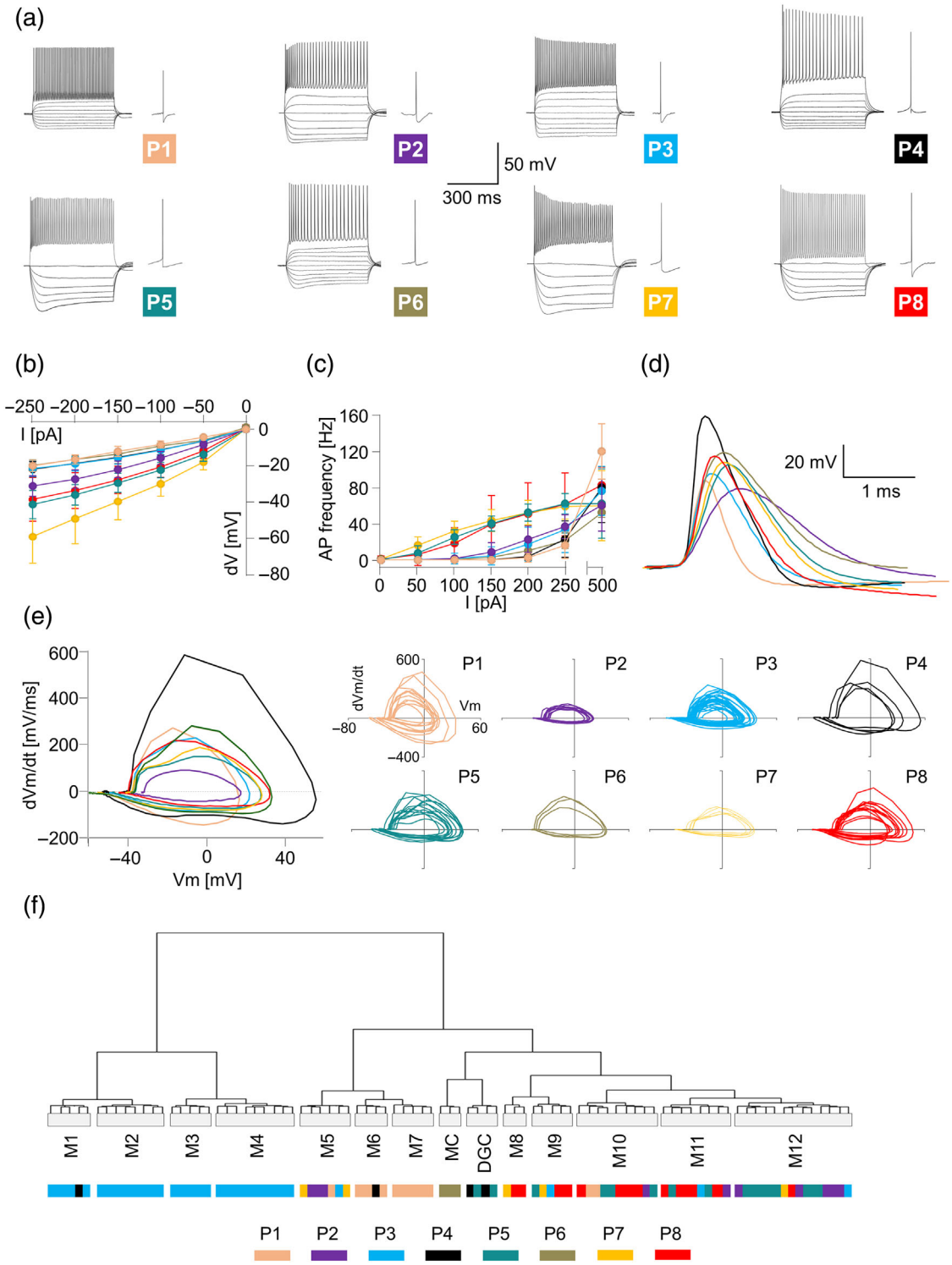

FIGURE 4 Electrophysiological properties of identified P-clusters and comparison with the morphological cluster result. (a) Voltage responses to a set of hyper- to depolarizing current pulses (−250 to 500 pA, 50 pA steps, 500 ms duration) with a representative single action potential (detail) elicited at rheobase. (b) *I/V*-plot of the different P-types (mean ± SD) revealed differences among clusters ($p < .0001$, two-way-ANOVA, P1: $N = 11$, P2: $N = 9$, P3: $N = 30$, P4: $N = 4$, P5: $N = 13$, P6: $N = 3$, P7: $N = 5$, P8: $N = 12$). (c) Current-firing response of the different P-types (mean ± SD) to a set of depolarizing current pulses revealed differences among clusters ($p < .0001$, two-way-ANOVA, P1: $N = 8$, P2: $N = 8$, P3: $N = 30$, P4: $N = 3$, P5: $N = 11$, P6: $N = 3$, P7: $N = 5$, P8: $N = 11$). (d, e) Representative AP voltage response (d, *aligned thresholds*) and phase plot (e, large panel) of a single neuron per P-cluster. Small panels in (e) show AP phase-plots of each neuron within the identified P-clusters. (f) Convergence of the morphological and physiological clusters of DG neurons. Dendrogram illustrates the morphological cluster result. Lower bars (color codes) represent the allocation of the individual physiologically identified (P-types) neurons to the morphologically identified clusters. M1-M12, morphological clusters M1-M12; P1-P8, physiological clusters P1-P8. DGC, dentate granule cell; MC, mossy cell

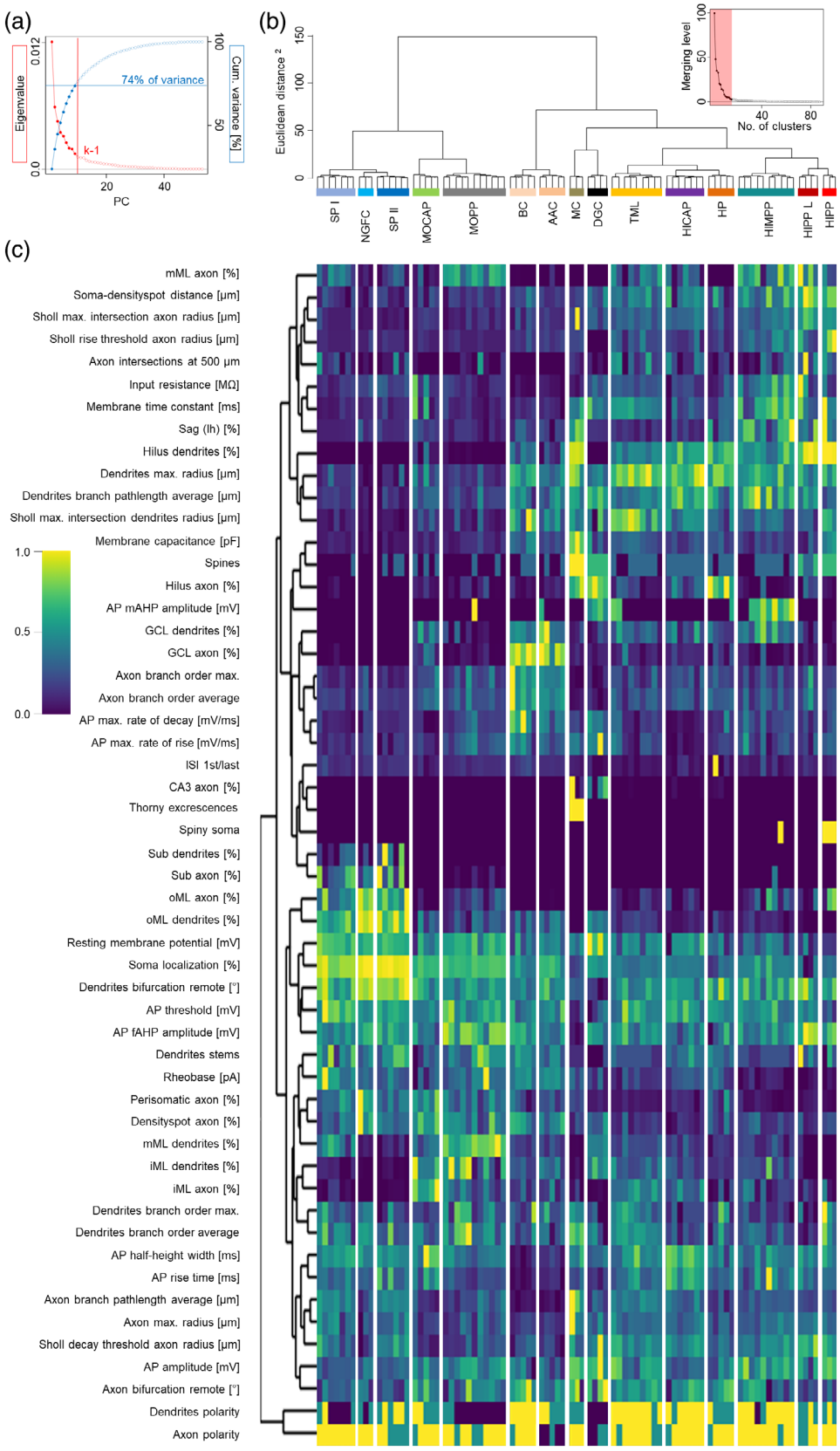

FIGURE 5 Legend on next page.

morphotypes possessed distinct physiological properties, others did not. In particular, the M6 and M7 morphotypes showed a high convergence with the P1 cluster reflecting the fast-spiking characteristic of these perisomatic-inhibitory INs. Likewise, the M8 morphotype showed a marked overlap with the P8 cluster. Importantly, P4 and P6 generally showed a good overlap with DGCs and MCs respectively, confirming the validity of their classification. However, most of the other morphotypes consisted of a variety of physiological types. A key distinguishing feature between morphotypes related to the P3 cluster, which generally overlapped with ML INs (M1–M4). This ML IN P-type generally had a V_m that was more hyperpolarized (−72.2 ± 6.0 mV) than P-types associated with hilar INs (−60.9 ± 7.2 mV). Finally, within hilar IN clusters, there was a loose overlap of morpho-physiological features, specifically M5 to P2, M11 to P8, and M12 to P2/P5. This analysis confirms that morphology and physiology alone are not sufficient to define distinct DG IN types, as such a combined approach is required.

3.5 | Combined morpho-physiological clustering reveals greater diversity of DG INs

As neither morphological nor physiological properties alone gave rise to a uniformly convergent IN classification, we next performed a combined morpho-physiological clustering which included all previously used descriptors. Performing KPCA followed by the scree-test, we identified nine principal components that constituted 74% of the observed variance (Figure 5a). Based on the principal components of this combined analysis, our HCA Ward revealed 15 distinct clusters of neurons following implementation of the "elbow-criterion" (Figure 5b, inset), which reflected the high IN diversity in the DG while also separating identified DGCs and MCs (Figure 5b) and was largely consistent with different clustering methods (k-means: 77% overlap; DIANA: 76% overlap, Figure S6). The relative magnitude of each parameter in relation to the identified morpho-physiological clusters is shown in Figure 5c with morpho-physiological parameters ordered by an independent Ward clustering. The result of this combined approach resembled that of the morphological clustering (Figure 2b), albeit with a number of previously classified IN types.

BCs ($N = 5$) and AACs ($N = 5$) contributed to two separate clusters, clearly representing discrete morpho-physiological IN types within the DG. Of the clustered BCs, all displayed the typical dense axonal arbor that ramified heavily around DGC somata and multipolar dendrites spanning the ML and extending deep into the hilus (Table 2). Their physiological characteristics comprised high-frequency trains of low-amplitude, fast APs in response to depolarizing current pulses, which were followed by large and fast AHPs. Typically, their V_m was depolarized, with low R_{in} and short membrane time-constants. In contrast, the AAC cluster displayed a similar dendritic distribution, but with somata predominantly found at the GCL/ML border and with cartridge-like axon collaterals oriented perpendicularly to the GCL/hilus border. Despite producing high-frequency trains of APs in response to depolarizing stimuli, AACs had slower AP kinetics, larger R_{in}, and lower C_m compared to BCs, which were the major separating physiological criteria (Tables 3 and 4). Nevertheless, BC and AAC clusters clearly segregated from the remaining hilar INs as emphasized by a large squared Euclidean distance of proportional 43.3%. This additionally highlights that BCs and AACs may occupy a unique niche in the DG network.

Other previously identified IN types included: (1) HIPP cells ($N = 3$), which had densely spiny somatodendritic domains localized to the hilus with axon projections to the outer two-thirds of the ML. HIPP cells showed a regular-spiking phenotype, with minimally adapting, large-amplitude APs and fast AHPs. Their V_m was depolarized, with relatively high R_{in} and long membrane time-constants. (2) HICAP cells ($N = 7$) with sparsely spiny dendrites spanning all layers of the DG and a characteristic axonal innervation of the iML. Hyperpolarized V_m, small voltage sag - indicating a low I_h - and highly adaptive trains of slow APs typified HICAP physiology. (3) TML cells ($N = 9$) which had hilar somata giving rise to multipolar, aspiny, or sparsely spiny dendrites and axons spanning all layers of the DG. TML AP trains showed strong adaptation with relatively fast AP kinetics, despite high R_{in}, and hyperpolarized V_m. (4) MOPP cells ($N = 11$), with somata and aspiny dendrites restricted to the ML and an axon that predominantly ramified in the outer two-thirds of the ML. MOPP cells possessed a pronounced hyperpolarized V_m, with low C_m and rapid membrane time-constants. MOPP AP discharge showed

FIGURE 5 IN classes of the DG based on a combined morpho-physiological hierarchical cluster analysis. (a) Eigenvalue/cumulative variance plot of the extracted principal components. Principal components that were retained for clustering ($N = 9$, *scree-test*, $k - 1$) are illustrated as red and blue circles together with the kink-point of the eigenvalue graph (k, red vertical line) and the contributed cumulative variance (blue horizontal line). (b) Dendrogram of the combined morpho-physiological cluster analysis obtained using Ward's minimum variance method. The 15 different clusters identified are illustrated by different colors. SP I: $N = 7$, NGFC: $N = 3$, SP II: $N = 6$, MOCAP: $N = 5$, MOPP: $N = 11$, BC: $N = 5$, AAC: $N = 5$, MC: $N = 3$, DGC: $N = 4$, TML: $N = 9$, HICAP: $N = 7$, HP: $N = 5$, HIMPP: $N = 10$, HIPP L: $N = 4$, HIPP: $N = 3$. Inset represents the inverse scree plot (no. of clusters/merging level) to define the optimal number of clusters that were maintained (*pale red* area) based on the inflection point of the graph (elbow-criterion). (c) Heatmap of the normalized morpho-physiological parameters plotted for each neuron (columns). Morpho-physiological parameters are ordered based on an independent Ward clustering. AAC, axo-axonic cell; AP, action potential; BC, basket cell; CA3, cornu ammonis 3; DGC, dentate granule cell; fAHP, fast after-hyperpolarization; GCL, granule cell layer; HICAP, hilar commissural–associational pathway associated cell; HIMPP, hilar medial perforant pathway associated cell; HIPP/ HIPP L, hilar perforant pathway associated (like) cell; HP, hilar projecting cell; iML, inner molecular layer; ISI, interspike interval; mAHP, medium after-hyperpolarization; MC, mossy cell; mML, middle molecular layer; MOCAP, molecular layer commissural–associational pathway associated cell; MOPP, molecular layer perforant pathway associated cell; NGFC, neurogliaform cell; oML, outer molecular layer; PC, principal component; SP I, subiculum projecting cell I; SP II, subiculum projecting cell II; Sub, subiculum; TML, total molecular layer cell

TABLE 2 Dendritic and axonal distribution of identified cell types

	Dendritic distribution (%)						Axonal distribution (%)						
Cell type (N)	Hilus	GCL	iML	mML	oML	Sub	CA3	Hilus	GCL	iML	mML	oML	Sub
SP I (7)			3.6 ± 2.5	30.1 ± 12.7	61.2 ± 12.2	5.1 ± 4.3		1.4 ± 2.8	0.7 ± 1.7	5.3 ± 7.0	28.2 ± 11.5	45.3 ± 19.7	19.0 ± 11.9
NGFC (3)			0.2 ± 0.3[a]	4.4 ± 1.7	93.2 ± 5.0	2.2 ± 3.5					4.6 ± 3.9	81.7 ± 9.3	13.8 ± 6.9
SP II (6)			0.8 ± 1.0	5.7 ± 4.9	82.6 ± 15.5	10.9 ± 11.0				0.8 ± 0.9	14.9 ± 11.7	64.6 ± 20.3	19.7 ± 16.6
MOCAP (5)	13.9 ± 16.0	10.9 ± 5.4	26.7 ± 11.5	23.3 ± 6.9	25.2 ± 18.4			8.1 ± 5.5	19.8 ± 12.7	61.4 ± 16.9	8.8 ± 11.1	1.9 ± 4.2	
MOPP (11)	0.8 ± 1.7	2.3 ± 3.6	24.0 ± 15.8	50.5 ± 8.6	22.5 ± 12.4		0.002 ± 0.01[a]	6.5 ± 8.7	2.8 ± 3.5	26.6 ± 12.3	44.8 ± 11.6	18.1 ± 10.7	1.2 ± 1.9
BC (5)	34.9 ± 10.2	13.1 ± 2.2	11.4 ± 3.1	13.1 ± 3.9	27.5 ± 13.8			5.8 ± 5.8	77.0 ± 7.8	17.1 ± 9.4	0.2 ± 0.2		
AAC (5)	19.6 ± 18.4	17.0 ± 9.2	15.9 ± 6.0	13.0 ± 4.8	34.6 ± 12.2			7.8 ± 4.6	69.7 ± 18.9	19.9 ± 14.1	2.5 ± 5.3	0.1 ± 0.3[a]	
MC (3)	92.0 ± 2.0	4.1 ± 3.3	1.1 ± 1.5	0.4 ± 0.4	0.1 ± 0.1[a]		11.6 ± 17.1	73.7 ± 16.4	7.6 ± 3.7	7.0 ± 9.4			
DGC (4)	0.03 ± 0.1[a]	4.1 ± 3.5	23.8 ± 6.8	30.0 ± 2.8	42.1 ± 7.9		12.7 ± 9.5	79.2 ± 12.0	7.3 ± 2.8	0.8 ± 1.2			
TML (9)	43.9 ± 7.1	9.3 ± 4.2	14.8 ± 5.6	16.3 ± 4.8	15.6 ± 5.5		0.04 ± 0.1[a]	13.8 ± 11.7	10.8 ± 11.4	37.2 ± 9.2	29.2 ± 16.3	8.9 ± 7.5	
HICAP (7)	60.1 ± 10.2	9.6 ± 6.0	10.6 ± 3.6	12.5 ± 5.5	7.3 ± 3.7		0.3 ± 0.5	28.8± 14.2	10.6 ± 3.8	30.5 ± 12.7	20.3 ± 14.9	9.6 ± 10.5	
HP (5)	68.2 ± 11.7	7.1 ± 3.6	6.4 ± 1.0	8.4 ± 4.5	10.0 ± 9.4		0.6 ± 0.7	76.6 ± 20.4	12.6 ± 10.7	10.2 ± 13.0	0.02 ± 0.04		
HIMPP (10)	52.1 ± 13.8	13.7 ± 5.9	13.1 ± 8.5	11.8 ± 5.7	9.4 ± 5.5			5.8 ± 10.8	6.1 ± 9.2	19.2 ± 12.9	44.4 ± 20.0	22.8 ± 21.4	1.6 ± 5.2[a]
HIPP L (4)	90.9 ± 12.4	4.5 ± 3.8	1.2 ± 2.4[a]	2.4 ± 4.8[a]	0.9 ± 1.9[a]			19.6 ± 15.3	4.5 ± 3.4	9.1 ± 8.3	53.3 ± 26.4	13.5 ± 17.7	
HIPP (3)	99.5 ± 0.9	0.5 ± 0.9[a]						3.8 ± 2.8	3.6 ± 3.9	14.6 ± 20.6	25.6 ± 12.9	52.3 ± 39.8	

Note: A summary of the percentage of dendritic and axonal arbors measured in the different layers of the DG and CA3. Data are shown as mean ± SD. Table entries are shaded grey when dendrites or axons were absent from a given layer.

Abbreviations: AAC, axo-axonic cell; BC, basket cell; CA3, cornu ammonis 3; DGC, dentate granule cell; GCL, granule cell layer; HICAP, hilar commissural–associational path associated cell; HIMPP, hilar medial-perforant-path associated cell; HIPP/ HIPP L, hilar perforant-path associated (like) cell; HP, hilar projecting cell; iML, inner molecular layer; MC, mossy cell; mML, middle molecular layer; MOCAP, molecular layer commissural–associational pathway associated cell; MOPP, molecular-layer perforant-path associated cell; NGFC, neurogliaform cell; oML, outer molecular layer; SP I, subiculum projecting cell I; SP II, subiculum projecting cell II; Sub, subiculum; TML, total molecular layer cell.

[a]$N = 1$ with a value other than 0.

TABLE 3 Passive membrane properties of identified cells types

Cell type (*N*)	Resting membrane potential (V_m) (mV)	Input resistance (R_{in}) (MΩ)	Membrane capacitance (C_m) (pF)	Membrane time-constant (ms)	Sag (I_h) (%)
SP I (7)	−76.1 ± 3.7	153.5 ± 35.6	56.8 ± 8.1	8.9 ± 2.0	2.8 ± 0.4
NGFC (3)	−72.6 ± 2.6	212.9 ± 38.8	40.9 ± 7.1	9.4 ± 0.9	5.8 ± 3.3
SP II (6)	−73.3 ± 2.1	220.6 ± 47.8	46.5 ± 9.1	10.7 ± 2.3	4.1 ± 1.3
MOCAP (5)	−63.2 ± 9.0	287.4 ± 193.6	63.7 ± 11.5	20.0 ± 14.8	6.2 ± 2.0
MOPP (11)	−71.4 ± 4.7	151.0 ± 42.8	63.6 ± 13.6	9.6 ± 2.5	3.2 ± 1.5
BC (5)	−60.5 ± 8.8	76.6 ± 19.4	128.8 ± 29.8	10.3 ± 2.1	6.4 ± 3.3
AAC (5)	−63.9 ± 4.3	92.8 ± 22.3	87.1 ± 11.3	8.7 ± 2.4	4.8 ± 2.8
MC (3)	−64.1 ± 4.4	108.5 ± 28.9	245.1 ± 35.5	25.4 ± 6.0	20.2 ± 4.5
DGC (4)	−80.2 ± 9.0	253.6 ± 49.6	107.5 ± 55.2	25.3 ± 8.5	4.1 ± 0.3
TML (9)	−63.9 ± 6.1	241.7 ± 25.9	106.5 ± 17.8	25.7 ± 3.5	3.8 ± 1.4
HICAP (7)	−65.5 ± 9.9	169.1 ± 59.4	86.4 ± 18.3	14.8 ± 5.4	3.8 ± 2.5
HP (5)	−58.7 ± 6.4	173.3 ± 85.2	94.3 ± 18.3	15.5 ± 4.8	9.7 ± 5.7
HIMPP (10)	−59.2 ± 5.7	384.0 ± 119.5	78.4 ± 15.2	29.8 ± 9.5	16.4 ± 7.7
HIPP L (4)	−55.3 ± 8.0	376.7 ± 268.3	74.3 ± 31.1	23.6 ± 11.0	13.6 ± 7.8
HIPP (3)	−51.8 ± 0.4	214.3 ± 121.8	155.1 ± 18.6	31.3 ± 13.9	16.9 ± 10.1

Note: A summary of the key passive membrane properties of morpho-physiological cell types identified in this study. Data are shown as mean ± SD. Abbreviations: AAC, axo-axonic cell; BC, basket cell; DGC, dentate granule cell; HICAP, hilar commissural–associational path associated cell; HIMPP, hilar medial-perforant-path associated cell; HIPP/ HIPP L, hilar perforant-path associated (like) cell; HP, hilar projecting cell; MC, mossy cell; MOCAP, molecular layer commissural–associational pathway associated cell; MOPP, molecular-layer perforant-path associated cell; NGFC, neurogliaform cell; SP I, subiculum projecting cell I; SP II, subiculum projecting cell II; TML, total molecular layer cell.

a regular-spiking nature, no adaptation, and large, fast AHPs. (5) NGFCs ($N = 3$), characterized by small somata located in the oML, gave rise to multiple short, profusely branching, aspiny dendrites that were locally restricted. The axon of NGFCs was extremely dense, and locally restricted. NGFCs possessed hyperpolarized V_m, short membrane time-constants, and the lowest C_m of any IN cluster—well reflecting their compact morphology. Their AP discharge pattern was uniformly regular-spiking, with no adaptation and small AP amplitudes.

Beyond these previously described types, the combined cluster analysis also revealed a number of novel IN types, which we have named based on the previously used nomenclature for DG INs (Freund & Buzsáki, 1996; Han et al., 1993). These new types are as follows:

Subiculum Projecting I (SP, cluster M1, M3–M4; cluster P3) cells: SP I cells ($N = 7$) were found in the outer two-thirds of the ML, with broad preference to the mML. They displayed predominantly monopolar aspiny dendrites with branches mostly found in the mML (30.1 ± 12.7% of dendrites) and oML (61.2 ± 12.2% of dendrites), but occasionally crossing the hippocampal fissure into the subiculum/CA1 (5.1 ± 4.3% of dendrites). Their multipolar axon projections covered all layers of the ML, with the majority localised to the mML (28.2 ± 11.5% of axon) and oML (45.3 ± 19.7% of axon). Characteristically, their axon showed numerous collaterals in the subiculum/CA1 region (19.0 ± 11.9% of axon). SP I cells had a hyperpolarized V_m (−76.1 ± 3.7 mV), a relatively low R_{in} (153.5 ± 35.6 MΩ) and a short membrane time-constant (8.9 ± 2.0 ms). They fired small and slow APs (AP amplitude: 49.8 ± 3.2 mV; half-height duration: 0.88 ± 0.10 ms) with depolarised voltage thresholds (−28.9 ± 3.7 mV).

Subiculum Projecting II (SP, cluster M4; cluster P3) cells: Similar to SP I cells, the SP II type ($N = 6$) was characterized by its prominent axonal projection into the subiculum/CA1. However, these INs had relatively small somata located to the oML in the immediate vicinity of the hippocampal fissure, which gave rise to radial, aspiny, or sparsely spiny dendrites primarily in the oML (82.6 ± 15.5% of dendrites), which also crossed the hippocampal fissure into the subiculum/CA1 (10.9 ± 11.0% of dendrites). In contrast to SP I neurons, SP II cells possessed a predominant horizontally oriented axon which extended over both the supra-and infra-pyramidal blades of the DG (max. axon radius: 576.7 ± 115.5 μm) and was present in the oML (64.6 ± 20.3% of axon), subiculum/CA1 (19.7 ± 16.6% of axon) and to a lesser extent in the mML (14.9 ± 11.7% of axon). SP II cells displayed a strongly hyperpolarized V_m (−73.3 ± 2.1 mV), short membrane time-constants (10.7 ± 2.3 ms), and a low C_m (46.5 ± 9.1 pF). Discharge properties of the SP II type revealed non-adapting (ISI first/last: 1.04 ± 0.09) trains of low amplitude and slow APs (AP amplitude: 51.0 ± 3.1 mV; half-height duration: 0.83 ± 0.06 ms).

Molecular Layer Commissural–Associational Pathway associated (MOCAP, cluster M5; cluster P2–P3, P7) cells: MOCAP cells ($N = 5$) were characterized by somata located exclusively in the iML, with aspiny or sparsely spiny bipolar dendritic trees that covered all layers of the DG. The distinctive characteristic of MOCAP cells was that their axon projected primarily to the iML (61.4 ± 16.9% of axon), co-aligned with the commissural–associational pathway similar to HICAP cells. Unlike other ML IN classes, MOCAP cells displayed a moderately hyperpolarized V_m (−63.2 ± 9.0 mV), a high R_{in} (287.4 ± 193.6 MΩ)

TABLE 4 Action potential properties of identified cell types

Cell type (N)	AP threshold (mV)	Rheobase (pA)	AP amplitude (mV)	AP max. rate of rise (mV/ms)	AP max. rate of decay (mV/ms)	AP rise time (RT) (ms)	AP half-height width (ms)	AP fAHP amplitude (mV)	AP mAHP amplitude (mV)	AP adaptation ratio (ISI first/last)[b]	AP discharge frequency at 250 pA (Hz)
SP I (7)	−28.9 ± 3.7	293.3 ± 105.4	49.8 ± 3.2	170.6 ± 21.1	63.0 ± 13.3	0.20 ± 0.03	0.88 ± 0.10	−15.8 ± 1.9		1.05 ± 0.27	11.8 ± 19.3
NGFC (3)	−34.1 ± 1.0	172.2 ± 21.4	54.5 ± 7.4	205.7 ± 32.9	74.2 ± 24.4	0.18 ± 0.01	0.81 ± 0.13	−19.3 ± 2.0		1.03 ± 0.18	59.1 ± 8.9
SP II (6)	−32.1 ± 1.5	168.1 ± 53.3	51.0 ± 3.1	165.2 ± 46.8	68.9 ± 4.7	0.23 ± 0.07	0.83 ± 0.06	−18.0 ± 2.6		1.04 ± 0.09	54.2 ± 29.1
MOCAP (5)	−35.7 ± 1.4	121.3 ± 80.2	58.0 ± 8.5	175.5 ± 40.2	55.1 ± 16.9	0.24 ± 0.06	1.03 ± 0.28	−14.1 ± 3.6		0.73 ± 0.29	51.3 ± 16.4
MOPP (11)	−32.0 ± 3.4	217.0 ± 102.2	61.9 ± 7.5	262.7 ± 58.4	88.0 ± 20.7	0.17 ± 0.02	0.73 ± 0.11	−21.7 ± 4.1	−1.9 ± 6.4[a]	0.96 ± 0.12	27.6 ± 16.4
BC (5)	−35.3 ± 3.4	232.7 ± 44.4	51.5 ± 12.5	311.8 ± 103.2	176.5 ± 69.4	0.11 ± 0.01	0.36 ± 0.08	−18.6 ± 2.3		1.20 ± 0.30	26.4 ± 32.5
AAC (5)	−33.8 ± 3.7	246.0 ± 31.4	48.7 ± 8.7	258.7 ± 44.1	128.4 ± 27.3	0.13 ± 0.02	0.43 ± 0.07	−14.4 ± 2.3	−2.6 ± 5.9[a]	0.96 ± 0.04	30.0 ± 21.3
MC (3)	−41.7 ± 2.6	161.1 ± 51.0	75.3 ± 4.4	301.0 ± 59.7	79.9 ± 15.8	0.18 ± 0.03	0.84 ± 0.16	−6.6 ± 0.8		0.64 ± 0.11	21.6 ± 9.3
DGC (4)	−40.0 ± 4.4	110.8 ± 65.8	74.4 ± 12.8	407.5 ± 166.4	133.2 ± 29.3	0.14 ± 0.02	0.65 ± 0.08	−16.5 ± 3.0	−12.0 ± 2.9	0.47 ± 0.30	47.5 ± 24.6
TML (9)	−33.4 ± 4.0	97.8 ± 38.7	64.4 ± 12.1	224.9 ± 77.5	82.1 ± 25.1	0.21 ± 0.04	0.82 ± 0.17	−16.8 ± 2.9	−3.5 ± 6.9	0.54 ± 0.13	46.5 ± 9.9
HICAP (7)	−32.5 ± 3.4	145.7 ± 32.6	50.5 ± 3.9	121.8 ± 20.0	52.0 ± 9.0	0.28 ± 0.04	1.05 ± 0.11	−13.8 ± 3.0		0.63 ± 0.32	31.8 ± 15.8
HP (5)	−34.0 ± 1.7	149.3 ± 66.0	54.8 ± 9.9	193.7 ± 26.8	85.7 ± 36.4	0.19 ± 0.02	0.72 ± 0.17	−12.7 ± 5.6	−2.5 ± 5.7[a]	1.57 ± 2.42	53.5 ± 53.8
HIMPP (10)	−34.4 ± 2.8	49.3 ± 27.7	67.1 ± 9.4	233.9 ± 86.8	96.4 ± 22.4	0.23 ± 0.07	0.73 ± 0.14	−15.9 ± 2.8	−12.8 ± 7.3	0.78 ± 0.40	60.7 ± 12.8
HIPP L (4)	−34.8 ± 1.7	35.0 ± 19.1	59.4 ± 13.8	203.3 ± 70.6	79.0 ± 17.8	0.21 ± 0.04	0.80 ± 0.13	−24.1 ± 4.0		0.85 ± 0.21	72.0 ± 22.9
HIPP (3)	−40.0 ± 2.4	35.6 ± 16.8	75.5 ± 3.0	269.5 ± 15.9	88.9 ± 24.0	0.20 ± 0.01	0.83 ± 0.16	−20.2 ± 3.9		0.80 ± 0.14	56.4 ± 0.4

Note: A summary of the key action-potential properties of morpho-physiological cell types identified in this study. Data are shown as mean ± SD. Table entries are shaded grey when mAHP was not observed in a given cell-type.

Abbreviations: SP I, subiculum projecting cell I; NGFC, neurogliaform cell; SP II, subiculum projecting cell II; MOCAP, molecular layer commissural–associational pathway associated cell; MOPP, molecular-layer perforant-path associated cell; BC, basket cell; AAC, axo-axonic cell; MC, mossy cell; DGC, dentate granule cell; TML, total molecular layer cell; HICAP, hilar commissural–associational path associated cell; HP, hilar projecting cell; HIMPP, hilar medial-perforant-path associated cell. HIPP/ HIPP L, hilar perforant-path associated (like) cell; AP, action potential; fAHP, fast after-hyperpolarization; mAHP, medium after-hyperpolarization; ISI, inter-spike interval.

[a]$N = 1$ with a value other than 0.

[b]At 250 pA, in $N = 11$, a pulse of 500 pA was required to elicit a train of APs.

and a long membrane time-constant (20.0 ± 14.8 ms). The AP discharge pattern revealed an adaptation (ISI first/last: 0.73 ± 0.29) with slow AP kinetics (half-height duration: 1.03 ± 0.28 ms).

HIPP Like (HIPP L, cluster M9; cluster P3, P7–P8) cells: These cells ($N = 4$) showed similarity to HIPP cells with respect to the somatodendritic and axonal distributions, with horizontally oriented somata in the hilus, spiny dendrites exclusively restricted to the same layer (90.9 ± 12.4% of dendrites) and few dendrites reaching the GCL (4.5 ± 3.8% of dendrites). HIPP L cells projected mainly to the outer two-thirds of the ML (66.7 ± 25.5% of axon) with the highest proportion observed in the mML (53.3 ± 26.4% of axon), but unlike true HIPP cells also formed a substantial axon ramification in the hilus (19.6 ± 15.3% of axon). HIPP L cells generally displayed a more depolarized V_m (−55.3 ± 8.0 mV) and a large voltage sag in response to hyperpolarizing current pulses (13.6 ± 7.8% of max. voltage decrease at −250 pA). The AP discharge of HIPP L cells showed minimal adaptation (ISI first/last: 0.85 ± 0.21), with small amplitude APs (59.4 ± 13.8 mV) and large fast AHPs (−24.1 ± 4.0 mV).

Hilar Projecting (HP, cluster M10; cluster P1, P5, and P8) cells: HP cells ($N = 5$) had somata located in the hilus with sparsely spiny, radial dendrites extending to the ML. The axon of HP cells was mainly restricted to the hilus (76.6 ± 20.4% of axon) with few collaterals crossing the GCL (10.2 ± 13.0% of axon). The V_m of HP cells was relatively depolarized (−58.7 ± 6.4 mV) and they produced small-amplitude APs (54.8 ± 9.9 mV) with moderate kinetics (half-height duration: 0.72 ± 0.17 ms).

Hilus Medial Perforant Pathway associated (HIMPP, cluster M9–M10, M12; cluster P5, P7–P8) cells: The HIMPP cell type ($N = 10$) was characterized by somata located in the hilus with aspiny or sparsely spiny dendrites covering all layers of the DG (% of dendrites: Hilus: 52.1 ± 13.8; GCL: 13.7 ± 5.9; ML: 34.2 ± 14.0). Neurons of this class gave rise to an axon that preferentially innervated the mML (44.4 ± 20.0% of axon). Physiologically, HIMPP cells had a relatively depolarized V_m (−59.2 ± 5.7 mV), high R_{in} (384.0 ± 119.5 MΩ), and a long membrane time-constant (29.8 ± 9.5 ms). Their AP discharge pattern showed slight adaptation (ISI first/last: 0.78 ± 0.40), with intermediate AP kinetics (half-height duration: 0.73 ± 0.14 ms) and a large medium AHP (−12.8 ± 7.3 mV).

Finally, DGC ($N = 4$) and MC ($N = 3$) clusters clearly segregated from INs, reflecting the divergent morphological and physiological properties. Indeed, in terms of physiology, DGCs and MCs displayed a hyperpolarized V_m and longer membrane time-constants than the majority of DG INs. Furthermore, they displayed high AP voltage thresholds and in response to depolarization, elicited large-amplitude APs with a high degree of adaptation.

An overview of all morpho-physiologically identified neuronal clusters is presented in Figure 6 (see also Figures S10–S21) and their specific morphological and electrophysiological characteristics are outlined in Tables 2–4. Comparison of the morpho-physiological with the morphology-alone dendrogram identified some notable differences in cluster composition arising after the inclusion of physiological parameters. Such disparities were particularly apparent in the SP I, HICAP, and HIMPP classes. Large discrepancy to the combined morpho-physiological cluster result, however, was observed in the physiology-alone dendrogram with only P1, P3, and P6 revealing a high convergence to the identified IN classes (Figure S2). A detailed summary of all morphological and physiological characteristics of the identified morpho-physiological clusters can be found in Tables S2–S4 and Tables S7–S8 and Figure S9.

3.6 | Neurochemical marker expression in DG INs

To confirm the IN types we report possessed distinctive neurochemical marker expression, we performed immunohistochemical labeling of selected INs ($N = 64$). The expression of neurochemicals was homogenous in some classes, while others displayed greater heterogeneity (Figure 7). Specifically, the BC cluster showed uniform expression of PV (5/5 cells tested). Similarly, the AAC cluster was predominantly PV expressing (4/5 cells tested), but also contained a single (p)CCK expressing IN (1/5 cells tested). The SP II and MOPP clusters expressed neuronal nitric oxide synthase (nNOS, SP II: 4/4 cells tested; MOPP: 8/8 cells tested), while HIPP and HIPP L clusters displayed expression of SST (HIPP: 3/3 cells tested; HIPP L: 4/4 cells tested). HICAP cells contained (p)CCK (1/2 cells tested) and Calbindin (CB, 1/2 cells tested) which were also present among TML neurons (CB: 4/9 cells tested; (p)CCK: 3/9 cells tested) beside an additional co-expression of CB and neuropeptide Y (NPY) in this cluster (2/9 cells tested). While SP I and NGFC types uniformly expressed nNOS (SP I: 5/5 cells tested; NGFC: 2/2 cells tested), other neurochemicals were also co-expressed (SP I: NPY: 1/5 cells tested, Calretinin (CR): 1/5 cells tested; NGFC: NPY: 1/2 cells tested, CR: 1/2 cells tested). HP neurons displayed a dichotomous marker expression with 2/5 cells immunoreactive for PV and 3/5 cells for (p)CCK. MOCAP neurons were often immunoreactive for either (p)CCK (2/4 cells tested) or nNOS (2/4 cells tested). Finally, HIMPP neurons were the most neurochemically heterogeneous type and variably expressed nNOS (2/8 cells tested), (p)CCK (4/8 cells tested), and CB (2/8 cells tested) with co-expression of NPY (1/8 cells tested).

Comparison with the neurochemical marker distribution displayed by the morphological and physiological cluster results separately (Figure S3) revealed a similar molecular pattern of the morphological result whereas much higher neuropeptide diversity was observed among the physiological clusters.

4 | DISCUSSION

In this study, we show that DG INs are morphologically and physiologically diverse and can be classified into distinct types. However, analysis based on morphology or physiology alone is insufficient to describe the true diversity of DG INs. We reveal a more complete estimation of this diversity by combining these two parameter sets which reliably distinguished previously described IN types and demonstrated the existence of novel DG IN types.

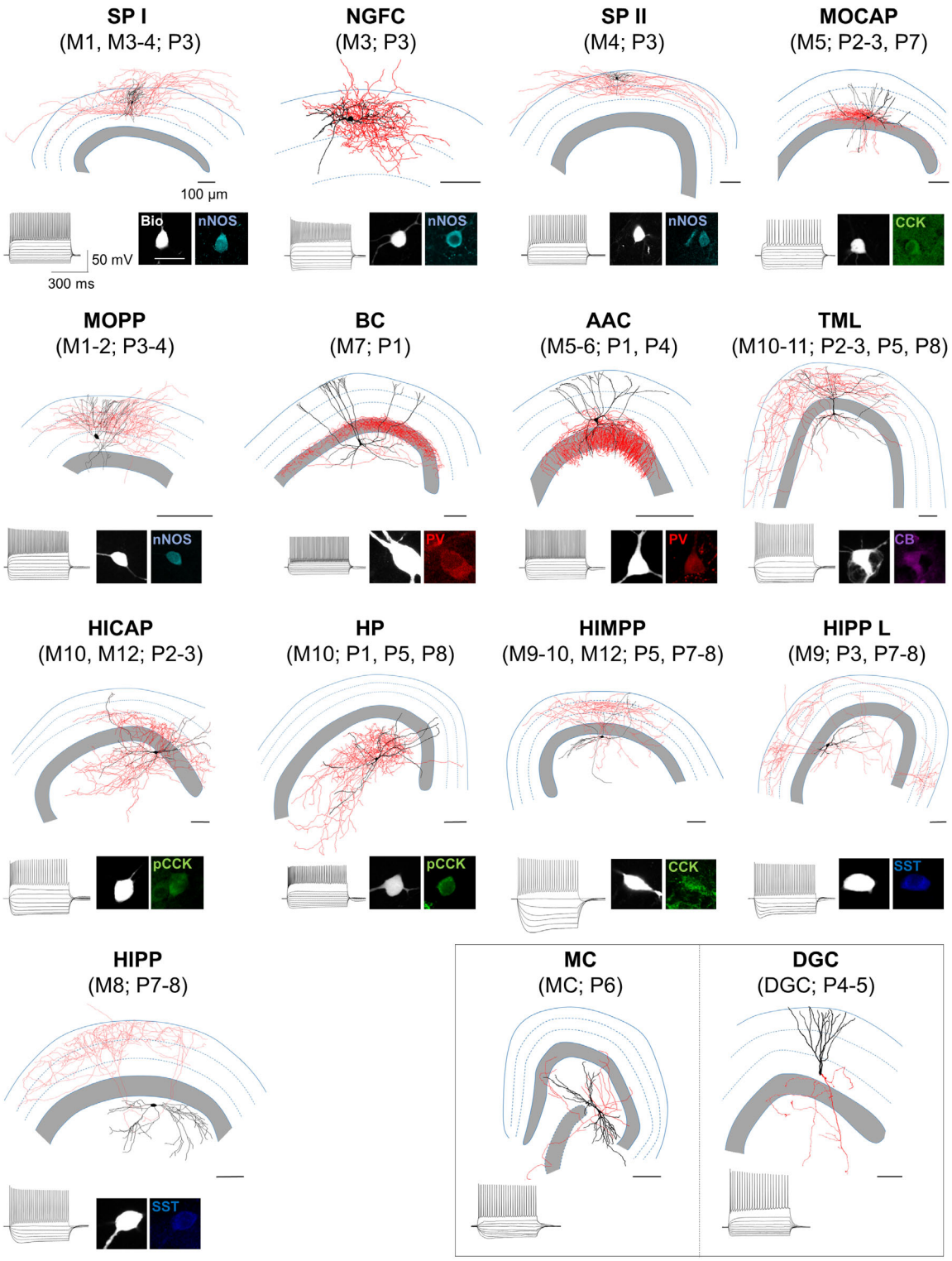

FIGURE 6 Illustration of the morpho-physiologically identified IN clusters in the DG. Representative reconstructions and voltage responses to a set of hyper- to depolarizing current pulses (50 pA steps, 500 ms duration) of each identified cluster. Soma and dendrites are shown in black, the axon in red. *Insets*, immunopositivity of the different IN clusters is shown together with the biocytin-filled soma. White scale bar: 20 µm. (p) CCK, (pro)-cholecystokinin; AAC, axo-axonic cell; BC, basket cell; Bio, biocytin; CB, calbindin; DGC, dentate granule cell; HICAP, hilar commissural–associational pathway associated cell; HIMPP, hilar medial perforant pathway associated cell; HIPP/ HIPP L, hilar perforant pathway associated (like) cell; HP, hilar projecting cell; MC, mossy cell; MOCAP, molecular layer commissural–associational pathway associated cell; MOPP, molecular layer perforant pathway associated cell; NGFC, neurogliaform cell; nNOS, neuronal nitric oxide synthase; PV, parvalbumin; SP I, subiculum projecting cell I; SP II, subiculum projecting cell II; SST, somatostatin; TML, total molecular layer cell

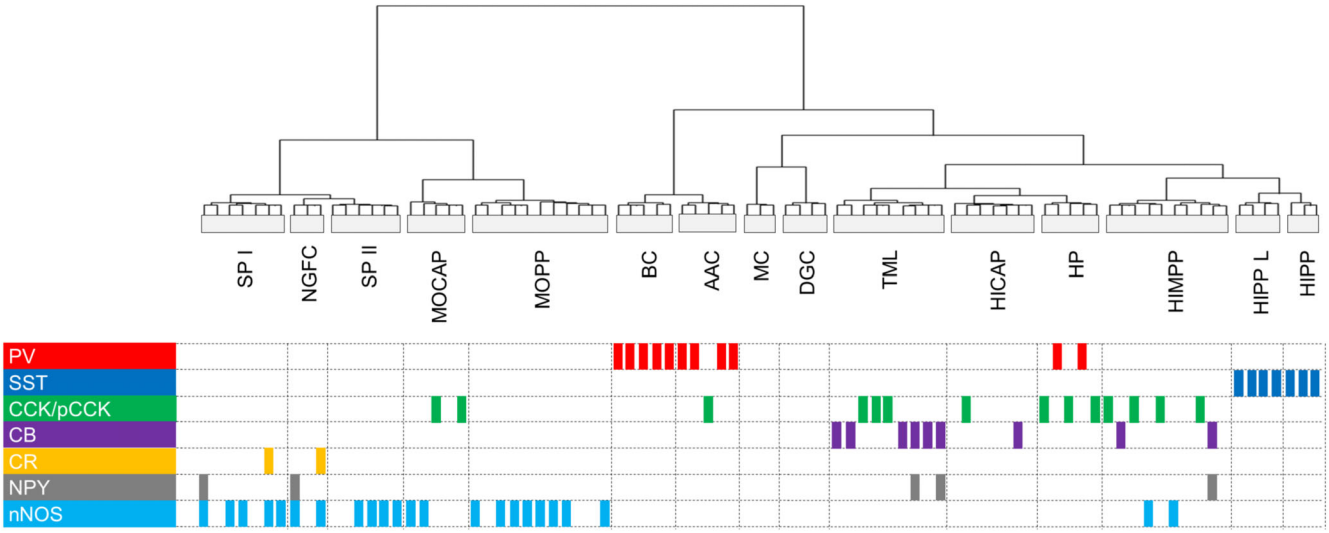

FIGURE 7 Correlation of the neurochemical marker expression with the morpho-physiologically identified IN clusters. Dendrogram represents the morpho-physiological cluster result using Ward's minimum variance method. Each immunopositive IN ($N = 64$) is represented by a colored bar in the row of the tested molecular marker (color-code). (p)CCK, (pro)cholecystokinin (green); AAC, axo-axonic cell; BC, basket cell; CB, calbindin (purple); CR, calretinin (yellow); DGC, dentate granule cell; HICAP, hilar commissural–associational pathway associated cell; HIMPP, hilar medial perforant pathway associated cell; HIPP/HIPP L, hilar perforant pathway associated (like) cell; HP, hilar projecting cell; MC, mossy cell; MOCAP, molecular layer commissural–associational pathway associated cell; MOPP, molecular layer perforant pathway associated cell; NGFC, neurogliaform cell; nNOS, neuronal nitric oxide synthase (light blue); NPY, neuropeptide Y (gray); PV, parvalbumin (red); SP I, subiculum projecting cell I; SP II, subiculum projecting cell II; SST, somatostatin (dark blue); TML, total molecular layer cell

4.1 | Morphology or physiology alone are insufficient to define DG IN diversity

A central assumption regarding neuronal diversity is that form follows function. As such, most studies examining IN diversity have defined and classified types based on their postsynaptic target specificity, represented by axon localization at the light microscopic level (Booker & Vida, 2018; Buhl et al., 1994; DeFelipe et al., 2013; Freund & Buzsáki, 1996; Han et al., 1993; Pelkey et al., 2017) and thus ultimately on their control of the local neuronal network and information transfer. With this in mind, we first sought to determine whether a purist anatomical approach alone was sufficient to describe DG IN diversity. Based on a reductionist morphological parameter space (20 axonal and 18 somatodendritic parameters), our analysis revealed 12 IN clusters of which 7 closely resembled previously described types (Armstrong et al., 2011; Freund & Buzsáki, 1996; Han et al., 1993; Hosp et al., 2014; Mott et al., 1997). However, some clusters showed heterogeneity and included multiple putative cell types.

Many studies, to date, have relied upon physiological properties of INs to confer identity, for example, fast-spiking versus regular-spiking IN classes (Druckmann et al., 2013). Using a reductionist classification method, as performed for morphology, we selected 15 passive and active electrophysiological parameters of neurons that represented the vast majority of IN diversity. However, subsequent clustering of INs based on these parameters only revealed eight physiological types, inconsistent with the result of the morphological approach. This finding is in good accord with previous studies that revealed physiology alone as a poor classifier of IN diversity (Gouwens et al., 2020; Hosp et al., 2014). Nevertheless, morphological and physiological classification of types did converge for at least certain IN types (M2–M4 with P3, M7 with P1). The remaining physiological types displayed a high degree of morphological diversity, in agreement with Mott et al., 1997, who showed that physiological parameters do not correlate well with axon distribution. That being said, physiological parameters were sufficient to distinguish hilar and ML INs, with V_m typically more hyperpolarized in latter types.

4.2 | Morpho-physiological clustering better reflects the diversity of DG INs

Our analysis of either morphology or physiology alone did not fully reflect the diversity of DG INs and could not fully separate known types. Recent studies have shown that a combined morpho-electrophysiological approach can better explain diversity (Gouwens et al., 2019; Hosp et al., 2014). As such, we employed a morpho-physiological clustering approach, based on the 53 morphological and electrophysiological parameters. This combined approach increased the number of identified IN clusters to 13, including previously undescribed IN types (Figures 5 and 6). Enhanced classification was noted in a number of morphotypes when physiology data was included, particularly in the M10 (INs with a major hilar projection) and M12 cluster what could not be dissected by morphology alone. Indeed, our combined cluster analysis identified most, if not all, previously described DG IN types (Han et al., 1993; Hosp et al., 2014; Mott et al., 1997), including BCs, AACs, HIPP cells, HICAP cells, TML cells,

NGFCs, and MOPP cells (with scattered atypical representatives observed among the latter type, that is, distinct hilar projection, i.e. Figure S14). However, comparing our morpho-physiological Ward's minimum variance method cluster result with a different clustering approach (k-means) revealed a high degree of correlation, but with merging of HICAP and TML types. Although characterized by distinct axonal distributions, these results could point out a larger morpho-physiological resemblance between these two IN classes than previously reported (Yu et al., 2015) which could be also indicated by their shared expression of (p)CCK and CB, observed in this study.

Furthermore, a number of novel IN types were identified, which included:

(1) SP I/II cells that possessed an axon predominantly located in the oML and also the subiculum, which likely correspond to cells described by Ceranik et al., 1997. However, this neuron class seems to comprise two distinct types. Besides major subiculum projections, observed in both types, SP I neurons had a more vertically oriented axon also occasionally extending into the hilus whereas SP II neurons revealed a more horizontal oriented axonal distribution restricted to the mML and oML. Differences were also apparent in their neuropeptide expression with SP I cells co-expressing NPY and CR together with nNOS in a subset of cells, compared to an exclusive nNOS expression in SP II neurons, indicating their potential molecular heterogeneity. Albeit not tested in the present study, these clusters may also comprise INs expressing vasoactive intestinal peptide (VIP), which have recently been shown as a diverse group in the DG, including a type with axon and dendrites extending into the subiculum (Wei et al., 2021).

(2) MOCAP cells possessed HICAP like axon lamination, but with somata localized to the ML and expressed (p)CCK or nNOS.

(3) HIMPP neurons had a layer-specific axonal distribution similar to that of HIPP cells albeit with an axon that was mainly restricted to the mML, co-aligned with the input from the medial EC (Dolorfo & Amaral, 1998; van Groen et al., 2003). Despite this specific axon alignment, HIMPP cells possessed diverse neuropeptide markers, potentially indicating diverse embryonic origins (Kepecs & Fishell, 2014; Tricoire et al., 2011).

(4) HIPP L cells, like the related HIPP cell type, had an axon preferentially in the outer two-thirds of the ML, most extensive within the mML and expressed SST, but, unlike HIPP cells, they also densely ramified in the hilus. This cell type is likely representing a variant of HIPP cells, but differs from the other SST neurons, HIL cells, recently described (Yuan et al., 2017), which have local axons restricted to the hilus and form long-range projections to the septal area.

(5) The cells, we identified as HP cells, with their somatodendritic and axonal localization confined to the hilus may reflect a closer approximation to HIL cells (Yuan et al., 2017). However, the dichotomous expression of (p)CCK or PV in our sample indicates a heterogeneity of these INs and may include BCs known to preferentially target MCs in the hilus (Acsády et al., 2000). Indeed, MCs and a subset of hilar INs have been reported to form a highly connected reciprocal network (Larimer & Strowbridge, 2008). In contrast, HIL cells have

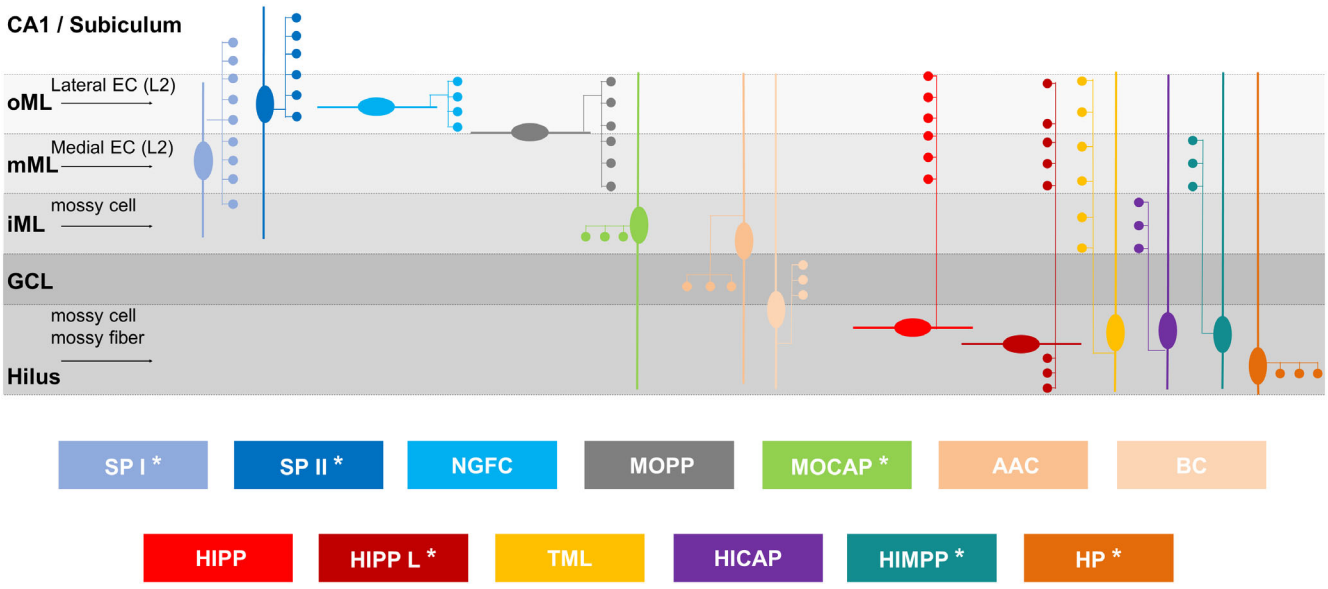

FIGURE 8 Synopsis of identified IN classes in the DG. Schematic overview of DG IN types superimposed on the layered structure of the DG (*gray*) with afferent pathways indicated by black arrows. Novel IN types are marked by an asterisk (*). Somato-dendritic distributions are illustrated by oval surfaces and thick lines, the axonal distribution is shown as thin lines and circles. AAC, axo-axonic cell; BC, basket cell; CA1, cornu ammonis 1; EC, entorhinal cortex; GCL, granule cell layer; HICAP, hilar commissural–associational pathway associated cell; HIMPP, hilar medial perforant pathway associated cell; HIPP/ HIPP L, hilar perforant pathway associated (like) cell; HP, hilar projecting cell (adapted and modified from Booker & Vida, 2018); iML, inner molecular layer; mML, middle molecular layer; MOCAP, molecular layer commissural–associational pathway associated cell; MOPP, molecular layer perforant pathway associated cell; NGFC, neurogliaform cell; oML, outer molecular layer; SP I, subiculum projecting cell I; SP II, subiculum projecting cell II; TML, total molecular layer cell

been shown to preferentially target other INs (Yuan et al., 2017) underscoring the anatomical heterogeneity of hilar IN types. Nevertheless, given the partial co-expression of PV and SST in INs from other hippocampal regions (Booker et al., 2018; Nassar et al., 2015), HIL cells may be present among our PV expressing sample of HP cells.

Thus, by using a combined morpho-physiological clustering approach, we could identify previously defined IN classes and several new IN types, in an objective, unbiased manner. Intriguingly, the novel IN types displayed an axonal projection that was aligned with at least one layer of the DG (Figure 8) emphasizing their functional implications in the hippocampal microcircuit.

Our study sought to provide a detailed characterization of DG INs by combining a large morpho-physiological parameter set with an unsupervised cluster analysis. Such an extensive parameter set potentially risks overfitting a given model. Therefore, we applied a KPCA to overcome the confounds of multidimensionality by reducing the input variable dimensions. The relatively low KMO values we report, together with the initial large parameter set may bias the outcome of our cluster analyses with regard to the revealed cluster structures. Nevertheless, the fact that we could clearly segregate PrCs from INs, not to mention previously identified IN classes, supports the validity of our proposed model.

Besides the analytical limitation, our estimate of IN diversity is almost certainly an underestimate, as we could not identify long-range projection INs (Eyre & Bartos, 2019; Melzer et al., 2012; Yuan et al., 2017), which possess axons cut during brain slicing. Furthermore, several previously identified IN types were not detected in our study, for example, CCK BCs (Hájos et al., 1996), nor did we assess a full range of neurochemical markers, as such may have overlooked important classifications, such as the various types of VIP/CR INs (Acsády et al., 1996; Hájos et al., 1996; Wei et al., 2021). Additionally, while this study provides a detailed morpho-physiological characterization of 80 INs, greater sampling may elucidate further functional diversity. Indeed, combining whole-cell recordings and RNA-sequencing (Cadwell et al., 2017) with the assessment of morphological, physiological, and transcriptomic features of neurons (Gouwens et al., 2020; Que et al., 2021; Scala et al., 2020) may allow greater determination of diversity.

4.3 | Functional ramifications of increased DG IN diversity

The DG serves as a principal gateway to the hippocampal formation, transforming the high frequency, dense neural code from the EC into sparsified, orthogonal information for the downstream Cornu Ammonis (Hainmueller & Bartos, 2020). This information transfer relies on the formation of stable ensembles of local DGCs, MCs, and INs to process this incoming synaptic information (Hainmueller & Bartos, 2018) in an afferent specific manner with respect to lateral versus medial EC—which separately encode spatial and egocentric or non-spatial information, respectively (Hunsaker et al., 2007; Sewards & Sewards, 2003; Witter et al., 2000). Previous studies have shown that multiple IN types have their inputs and outputs aligned with such specific paths, such as HICAP cells whose axon co-terminates with associative inputs in the iML or HIPP cells innervating the oML, which receives lateral EC inputs. Important to such afferent specific alignment is where IN dendritic fields align, such that HICAP and HIPP cells may be considered predominantly feedback INs. The newly described HIPP L, HIMPP and MOCAP cells add to this diversity- and layer-specific control. HIPP L and HIMPP cells specifically co-terminate with medial EC inputs and thus may specifically control the spatial code in a feed-forward and feedback manner given their diverse dendritic distribution. In contrast, MOCAP cells co-terminate with associative inputs, but likely produce such inhibition in a feed-forward manner.

Furthermore, the greater diversity of INs we described has implications for the activation of GABAergic receptors by a given IN type. In DGCs slow $GABA_B$-receptors are preferentially localized to the distal dendrites in the mML and oML (Degro et al., 2015), contributing to activity-dependent and tonic inhibition of these PrCs (Gonzalez et al., 2018). The layer-specific and dense localization of the axon from these newly described and previously known DG INs will have direct ramifications on the spatiotemporal dynamics of GABAergic signaling achieved in both mature and immature DGCs (Markwardt et al., 2009). This further highlights the role of multiple IN classes for synaptic plasticity at a circuit level (Sambandan et al., 2010) and the profile of inhibition between PrCs and INs within the DG circuit more generally (Bartos et al., 2011).

ACKNOWLEDGMENTS

We would like to thank Ina Wolter and Heike Heilmann for their excellent technical support and to members of the Vida Lab for helpful comments and discussion. This work was funded by the Deutche Forschungsgemeinschaft (DFG, Grant: EXC 257, FOR 2143 to Imre Vida).

CONFLICT OF INTEREST

The authors state that they have no competing financial interests.

DATA AVAILABILITY STATEMENT

The data that support the findings of this study are available from the corresponding author upon reasonable request.

ORCID

Imre Vida https://orcid.org/0000-0003-3214-2233
Sam A. Booker https://orcid.org/0000-0003-1980-9873

REFERENCES

Acsády, L., Arabadzisz, D., & Freund, T. F. (1996). Correlated morphological and neurochemical features identify different subsets of vasoactive intestinal polypeptide-immunoreactive interneurons in rat hippocampus. *Neuroscience*, *73*(2), 299–315. https://doi.org/10.1016/0306-4522(95)00610-9

Acsády, L., Katona, I., Martínez-Guijarro, F. J., Buzsáki, G., & Freund, T. F. (2000). Unusual target selectivity of perisomatic inhibitory cells in the hilar region of the rat hippocampus. *Journal of Neuroscience*, *20*(18), 6907–6919. https://doi.org/10.1523/jneurosci.20-18-06907.2000

Amaral, D. G., Scharfman, H. E., & Lavenex, P. (2007). The dentate gyrus: Fundamental neuroanatomical organization (dentate gyrus for dummies). *Progress in Brain Research*, *163*, 3–22. https://doi.org/10.1016/S0079-6123(07)63001-5

Andersen, P., Bland, B. H., & Dudar, J. D. (1973). Organization of the hippocampal output. *Experimental Brain Research*, *17*(2), 152–168. https://doi.org/10.1007/BF00235025

Armstrong, C., Krook-Magnuson, E., & Soltesz, I. (2012). Neurogliaform and ivy cells: A major family of nNOS expressing GABAergic neurons. *Frontiers in Neural Circuits*, *6*(May), 1–10. https://doi.org/10.3389/fncir.2012.00023

Armstrong, C., Szabadics, J., Tamás, G., & Soltesz, I. (2011). Neurogliaform cells in the molecular layer of the dentate gyrus as feed-forward γ -aminobutyric acidergic modulators of entorhinal-hippocampal interplay. *Journal of Comparative Neurology*, *519*(8), 1476–1491. https://doi.org/10.1002/cne.22577

Bacher, J., Pöge, A., & Wenzig, K. (2010). *Clusteranalyse*. Oldenbourg. https://doi.org/10.1524/9783486710236

Bartlett, M. S. (1950). Tests of significance in factor analysis. *British Journal of Statistical Psychology*, *3*(2), 77–85. https://doi.org/10.1111/j.2044-8317.1950.tb00285.x

Bartos, M., Alle, H., & Vida, I. (2011). Role of microcircuit structure and input integration in hippocampal interneuron recruitment and plasticity. *Neuropharmacology*, *60*(5), 730–739. https://doi.org/10.1016/j.neuropharm.2010.12.017

Bartos, M., Vida, I., & Jonas, P. (2007). Synaptic mechanisms of synchronized gamma oscillations in inhibitory interneuron networks. *Nature Reviews Neuroscience*, *8*(1), 45–56. https://doi.org/10.1038/nrn2044

Bolduan, F., Grosser, S., & Vida, I. (2020). Minimizing shrinkage of acute brain slices using metal spacers during histological embedding. *Brain Structure and Function*, *225*(8), 2577–2589. https://doi.org/10.1007/s00429-020-02141-3

Booker, S. A., Loreth, D., Gee, A. L., Watanabe, M., Kind, P. C., Wyllie, D. J. A., Kulik, A., & Vida, I. (2018). Postsynaptic GABABRs inhibit L-type calcium channels and abolish long-term potentiation in hippocampal somatostatin interneurons. *Cell Reports*, *22*(1), 36–43. https://doi.org/10.1016/j.celrep.2017.12.021

Booker, S. A., Song, J., & Vida, I. (2014). Whole-cell patch-clamp recordings from morphologically- and Neurochemically-identified hippocampal interneurons. *Journal of Visualized Experiments*, *91*, e51706. https://doi.org/10.3791/51706

Booker, S. A., & Vida, I. (2018). Morphological diversity and connectivity of hippocampal interneurons. *Cell and Tissue Research*, *373*(3), 619–641. https://doi.org/10.1007/s00441-018-2882-2

Buhl, E. H., Halasy, K., & Somogyi, P. (1994). Diverse sources of hippocampal unitary inhibitory postsynaptic potentials and the number of synaptic release sites. *Nature*, *368*(6474), 823–828. https://doi.org/10.1038/368823a0

Buzsáki, G. (1984). Feed-forward inhibition in the hippocampal formation. In. *Progress in Neurobiology*, *22*(2), 131–153. https://doi.org/10.1016/0301-0082(84)90023-6

Cadwell, C. R., Scala, F., Li, S., Livrizzi, G., Shen, S., Sandberg, R., Jiang, X., & Tolias, A. S. (2017). Multimodal profiling of single-cell morphology, electrophysiology, and gene expression using patch-seq. *Nature Protocols*, *12*(12), 2531–2553. https://doi.org/10.1038/nprot.2017.120

Cattell, R. B. (1966). The scree test for the number of factors. *Multivariate Behavioral Research*, *1*(2), 245–276. https://doi.org/10.1207/s15327906mbr0102_10

Ceranik, K., Bender, R., Geiger, J. R., Monyer, H., Jonas, P., Frotscher, M., & Lübke, J. (1997). A novel type of GABAergic interneuron connecting the input and the output regions of the hippocampus. *The Journal of Neuroscience*, *17*(14), 5380–5394.

DeFelipe, J., López-Cruz, P. L., Benavides-Piccione, R., Bielza, C., Larrañaga, P., Anderson, S., Burkhalter, A., Cauli, B., Fairén, A., Feldmeyer, D., Fishell, G., Fitzpatrick, D., Freund, T. F., González-Burgos, G., Hestrin, S., Hill, S., Hof, P. R., Huang, J., Jones, E. G., … Ascoli, G. A. (2013). New insights into the classification and nomenclature of cortical GABAergic interneurons. *Nature Reviews Neuroscience*, *14*(3), 202–216. https://doi.org/10.1038/nrn3444

Degro, C. E., Kulik, A., Booker, S. A., & Vida, I. (2015). Compartmental distribution of gabab receptor-mediated currents along the somatodendritic axis of hippocampal principal cells. *Frontiers in Synaptic Neuroscience*, *7*(MAR), 6. https://doi.org/10.3389/fnsyn.2015.00006

Dolorfo, C. L., & Amaral, D. G. (1998). Entorhinal cortex of the rat: Topographic organization of the cells of origin of the perforant path projection to the dentate gyrus. *Journal of Comparative Neurology*, *398*(1), 25–48. https://doi.org/10.1002/(SICI)1096-9861(19980817)398:1<25::AID-CNE3>3.0.CO;2-B

Druckmann, S., Hill, S., Schürmann, F., Markram, H., & Segev, I. (2013). A hierarchical structure of cortical interneuron electrical diversity revealed by automated statistical analysis. *Cerebral Cortex (New York, N.Y.: 1991)*, *23*(12), 2994–3006. https://doi.org/10.1093/cercor/bhs290

Eyre, M. D., & Bartos, M. (2019). Somatostatin-expressing interneurons form axonal projections to the contralateral hippocampus. *Frontiers in Neural Circuits*, *13*, 56. https://doi.org/10.3389/fncir.2019.00056

Field, A. P. (2000). *Discovering statistics using SPSS for windows: Advanced techniques for the beginner*. Sage.

Freund, T. F., & Buzsáki, G. (1996). Interneurons of the hippocampus. *Hippocampus*, *6*(4), 347–470. https://doi.org/10.1002/(sici)1098-1063(1996)6:4<347::aid-hipo1>3.0.co;2-i

Gloveli, T., Dugladze, T., Saha, S., Monyer, H., Heinemann, U., Traub, R. D., Whittington, M. A., & Buhl, E. H. (2005). Differential involvement of oriens/pyramidale interneurones in hippocampal network oscillations in vitro. *Journal of Physiology*, *562*(1), 131–147. https://doi.org/10.1113/jphysiol.2004.073007

Gonzalez, J. C., Epps, S. A., Markwardt, S. J., Wadiche, J. I., & Overstreet-Wadiche, L. (2018). Constitutive and synaptic activation of GIRK channels differentiates mature and newborn dentate granule cells. *Journal of Neuroscience*, *38*(29), 6513–6526. https://doi.org/10.1523/JNEUROSCI.0674-18.2018

Gouwens, N. W., Sorensen, S. A., Baftizadeh, F., Budzillo, A., Lee, B. R., Jarsky, T., Alfiler, L., Baker, K., Barkan, E., Berry, K., Bertagnolli, D., Bickley, K., Bomben, J., Braun, T., Brouner, K., Casper, T., Crichton, K., Daigle, T. L., Dalley, R., … Zeng, H. (2020). Integrated Morphoelectric and transcriptomic classification of cortical GABAergic cells. *Cell*, *183*(4), 935–953.e19. https://doi.org/10.1016/j.cell.2020.09.057

Gouwens, N. W., Sorensen, S. A., Berg, J., Lee, C., Jarsky, T., Ting, J., Sunkin, S. M., Feng, D., Anastassiou, C. A., Barkan, E., Bickley, K., Blesie, N., Braun, T., Brouner, K., Budzillo, A., Caldejon, S., Casper, T., Castelli, D., Chong, P., … Koch, C. (2019). Classification of electrophysiological and morphological neuron types in the mouse visual cortex. *Nature Neuroscience*, *22*(7), 1182–1195. https://doi.org/10.1038/s41593-019-0417-0

Guzman, S. J., Schlögl, A., & Schmidt-Hieber, C. (2014). Stimfit: Quantifying electrophysiological data with python. *Frontiers in Neuroinformatics*, *8*(FEB), 16. https://doi.org/10.3389/fninf.2014.00016

Hainmueller, T., & Bartos, M. (2018). Parallel emergence of stable and dynamic memory engrams in the hippocampus. *Nature*, *558*(7709), 292–296. https://doi.org/10.1038/s41586-018-0191-2

Hainmueller, T., & Bartos, M. (2020). Dentate gyrus circuits for encoding, retrieval and discrimination of episodic memories. *Nature Reviews Neuroscience*, *21*(3), 153–168. https://doi.org/10.1038/s41583-019-0260-z

Hájos, N., Acsády, L., & Freund, T. F. (1996). Target selectivity and neurochemical characteristics of VIP-immunoreactive interneurons in the rat dentate gyrus. *European Journal of Neuroscience*, *8*(7), 1415–1431. https://doi.org/10.1111/j.1460-9568.1996.tb01604.x

Hájos, N., Ellender, T. J., Zemankovics, R., Mann, E. O., Exley, R., Cragg, S. J., Freund, T. F., & Paulsen, O. (2009). Maintaining network activity in submerged hippocampal slices: Importance of oxygen supply. *European Journal of Neuroscience*, *29*(2), 319–327. https://doi.org/10.1111/j.1460-9568.2008.06577.x

Han, Z. -S., Buhl, E. H., Lörinczi, Z., & Somogyi, P. (1993). A high degree of spatial selectivity in the axonal and dendritic domains of physiologically identified local-circuit neurons in the dentate gyms of the rat hippocampus. *European Journal of Neuroscience*, *5*(5), 395–410. https://doi.org/10.1111/j.1460-9568.1993.tb00507.x

Hines, M. L., & Carnevale, N. T. (1997). The NEURON simulation environment. *Neural Computation*, *9*(6), 1179–1209. https://doi.org/10.1162/neco.1997.9.6.1179

Hosp, J. A., Yanagawa, Y., Strüber, M., Obata, K., Vida, I., Jonas, P., & Bartos, M. (2014). Morpho-physiological criteria divide dentate gyrus interneurons into classes. *Hippocampus*, *24*(2), 189–203. https://doi.org/10.1002/hipo.22214

Hunsaker, M. R., Mooy, G. G., Swift, J. S., & Kesner, R. P. (2007). Dissociations of the medial and lateral Perforant path projections into dorsal DG, CA3, and CA1 for spatial and nonspatial (visual object) information processing. *Behavioral Neuroscience*, *121*(4), 742–750. https://doi.org/10.1037/0735-7044.121.4.742

Kaiser, H. F. (1974). An index of factorial simplicity. *Psychometrika*, *39*(1), 31–36. https://doi.org/10.1007/BF02291575

Karatzoglou, A., Hornik, K., Smola, A., & Zeileis, A. (2004). kernlab—An S4 package for kernel methods in R. *Journal of Statistical Software*, *11*, 1–20. https://doi.org/10.18637/jss.v011.i09

Kepecs, A., & Fishell, G. (2014). Interneuron cell types are fit to function. *Nature*, *505*(7483), 318–326. https://doi.org/10.1038/nature12983

Larimer, P., & Strowbridge, B. W. (2008). Nonrandom local circuits in the dentate gyrus. *Journal of Neuroscience*, *28*, 12212–12223.

Longair, M. H., Baker, D. A., & Armstrong, J. D. (2011). Simple neurite tracer: Open source software for reconstruction, visualization and analysis of neuronal processes. *Bioinformatics*, *27*(17), 2453–2454. https://doi.org/10.1093/bioinformatics/btr390

Markwardt, S. J., Wadiche, J. I., & Overstreet-Wadiche, L. S. (2009). Input-specific GABAergic signaling to newborn neurons in adult dentate gyrus. *Journal of Neuroscience*, *29*(48), 15063–15072. https://doi.org/10.1523/JNEUROSCI.2727-09.2009

Melzer, S., Michael, M., Caputi, A., Eliava, M., Fuchs, E. C., Whittington, M. A., & Monyer, H. (2012). Long-range-projecting gabaergic neurons modulate inhibition in hippocampus and entorhinal cortex. *Science*, *335*(6075), 1506–1510. https://doi.org/10.1126/science.1217139

Morris, R. G. M., Garrud, P., Rawlins, J. N. P., & O'Keefe, J. (1982). Place navigation impaired in rats with hippocampal lesions. *Nature*, *297*(5868), 681–683. https://doi.org/10.1038/297681a0

Mott, D. D., Turner, D. A., Okazaki, M. M., & Lewis, D. V. (1997). Interneurons of the dentate-hilus border of the rat dentate gyrus: Morphological and electrophysiological heterogeneity. *The Journal of Neuroscience*, *17*(11), 3990–4005.

Nassar, M., Simonnet, J., Lofredi, R., Cohen, I., Savary, E., Yanagawa, Y., Miles, R., & Fricker, D. (2015). Diversity and overlap of parvalbumin and somatostatin expressing interneurons in mouse presubiculum. *Frontiers in Neural Circuits*, *9*(May), 20. https://doi.org/10.3389/fncir.2015.00020

O'Keefe, J., & Dostrovsky, J. (1971). The hippocampus as a spatial map. Preliminary evidence from unit activity in the freely-moving rat. *Brain Research*, *34*(1), 171–175. https://doi.org/10.1016/0006-8993(71)90358-1

Pelkey, K. A., Chittajallu, R., Craig, M. T., Tricoire, L., Wester, J. C., & McBain, C. J. (2017). Hippocampal gabaergic inhibitory interneurons. *Physiological Reviews*, *97*(4), 1619–1747. https://doi.org/10.1152/physrev.00007.2017

Que, L., Lukacsovich, D., Luo, W., & Földy, C. (2021). Transcriptional and morphological profiling of parvalbumin interneuron subpopulations in the mouse hippocampus. *Nature Communications*, *12*(1), 108. https://doi.org/10.1038/s41467-020-20328-4

Ripley, B. D. (2001). The R project in statistical computing. *MSOR Connections*, *1*(1), 23–25. https://doi.org/10.11120/msor.2001.01010023

Sambandan, S., Sauer, J. F., Vida, I., & Bartos, M. (2010). Associative plasticity at excitatory synapses facilitates recruitment of fast-spiking interneurons in the dentate gyrus. *Journal of Neuroscience*, *30*(35), 11826–11837. https://doi.org/10.1523/JNEUROSCI.2012-10.2010

Scala, F., Kobak, D., Bernabucci, M., Bernaerts, Y., Cadwell, C. R., Castro, J. R., Hartmanis, L., Jiang, X., Laturnus, S., Miranda, E., Mulherkar, S., Tan, Z. H., Yao, Z., Zeng, H., Sandberg, R., Berens, P., & Tolias, A. S. (2020). Phenotypic variation of transcriptomic cell types in mouse motor cortex. *Nature*, *598*, 144–150. https://doi.org/10.1038/s41586-020-2907-3

Scharfman, H. E. (1995). Electrophysiological diversity of pyramidal-shaped neurons at the granule cell layer/hilus border of the rat dentate gyrus recorded in vitro. *Hippocampus*, *5*(4), 287–305. https://doi.org/10.1002/hipo.450050403

Schölkopf, B., Smola, A., & Müller, K. R. (1998). Nonlinear component analysis as a kernel eigenvalue problem. *Neural Computation*, *10*, 1299–1319. https://doi.org/10.1162/089976698300017467

Scorcioni, R., Polavaram, S., & Ascoli, G. A. (2008). L-measure: A web-accessible tool for the analysis, comparison and search of digital reconstructions of neuronal morphologies. *Nature Protocols*, *3*(5), 866–876. https://doi.org/10.1038/nprot.2008.51

Seress, L., & Ribak, C. E. (1983). GABAergic cells in the dentate gyrus appear to be local circuit and projection neurons. *Experimental Brain Research*, *50*(2–3), 173–182. https://doi.org/10.1007/BF00239181

Sewards, T. V., & Sewards, M. A. (2003). Input and output stations of the entorhinal cortex: Superficial vs. deep layers or lateral vs. medial divisions? *Brain Research Reviews*, *42*(3), 243–251. https://doi.org/10.1016/S0165-0173(03)00175-9

Sik, A., Penttonen, M., & Buzsáki, G. (1997). Lnterneurons in the hippocampal dentate gyrus: An in vivo intracellular study. *The European Journal of Neuroscience*, *9*(3), 573–588.

Somogyi, P., & Klausberger, T. (2005). Defined types of cortical interneurone structure space and spike timing in the hippocampus. *The Journal of Physiology*, *562*(Pt 1), 9–26. https://doi.org/10.1113/jphysiol.2004.078915

Sullivan, D., Csicsvari, J., Mizuseki, K., Montgomery, S., Diba, K., & Buzsáki, G. (2011). Relationships between hippocampal sharp waves, ripples, and fast gamma oscillation: Influence of dentate and entorhinal cortical activity. *Journal of Neuroscience*, *31*(23), 8605–8616. https://doi.org/10.1523/JNEUROSCI.0294-11.2011

Tricoire, L., Pelkey, K. A., Erkkila, B. E., Jeffries, B. W., Yuan, X., & McBain, C. J. (2011). A blueprint for the spatiotemporal origins of mouse hippocampal interneuron diversity. *Journal of Neuroscience*, *31*(30), 10948–10970. https://doi.org/10.1523/JNEUROSCI.0323-11.2011

Uematsu, M., Hirai, Y., Karube, F., Ebihara, S., Kato, M., Abe, K., Obata, K., Yoshida, S., Hirabayashi, M., Yanagawa, Y., & Kawaguchi, Y. (2008). Quantitative chemical composition of cortical GABAergic neurons revealed in transgenic venus-expressing rats. *Cerebral Cortex*, *18*(2), 315–330. https://doi.org/10.1093/cercor/bhm056

van Groen, T., Miettinen, P., & Kadish, I. (2003). The entorhinal cortex of the mouse: Organization of the projection to the hippocampal formation. *Hippocampus*, *13*(1), 133–149. https://doi.org/10.1002/hipo.10037

Vida, I., Bartos, M., & Jonas, P. (2006). Shunting inhibition improves robustness of gamma oscillations in hippocampal interneuron networks by homogenizing firing rates. *Neuron*, *49*(1), 107–117. https://doi.org/10.1016/j.neuron.2005.11.036

Wei, Y. T., Wu, J. W., Yeh, C. W., Shen, H. C., Wu, K. P., Vida, I., & Lien, C. C. (2021). Morpho-physiological properties and connectivity of vasoactive intestinal polypeptide-expressing interneurons in the

mouse hippocampal dentate gyrus. *The Journal of Comparative Neurology*, *529*, 2658–2675. https://doi.org/10.1002/cne.25116

Witter, M. P., Naber, P. A., Van Haeften, T., Machielsen, W. C. M., Rombouts, S. A. R. B., Barkhof, F., Scheltens, P., & Lopes Da Silva, F. H. (2000). Cortico-hippocampal communication by way of parallel parahippocampal-subicular pathways. *Hippocampus*, *10*(4), 398–410. https://doi.org/10.1002/1098-1063(2000)10:4<398::AID-HIPO6>3.0.CO;2-K

Ylinen, A., Bragin, A., Nadasdy, Z., Jando, G., Szabo, I., Sik, A., & Buzsáki, G. (1995). Sharp wave-associated high-frequency oscillation (200 Hz) in the intact hippocampus: Network and intracellular mechanisms. *Journal of Neuroscience*, *15*(1 I), 30–46. https://doi.org/10.1523/jneurosci.15-01-00030.1995

Yu, J., Swietek, B., Proddutur, A., & Santhakumar, V. (2015). Dentate total molecular layer interneurons mediate cannabinoid-sensitive inhibition. *Hippocampus*, *25*(8), 884–889. https://doi.org/10.1002/hipo.22419

Yuan, M., Meyer, T., Benkowitz, C., Savanthrapadian, S., Ansel-Bollepalli, L., Foggetti, A., Wulff, P., Alcami, P., Elgueta, C., & Bartos, M. (2017). Somatostatin-positive interneurons in the dentate gyrus of mice provide local- and long-range septal synaptic inhibition. *eLife*, *6*, e21105. https://doi.org/10.7554/elife.21105

SUPPORTING INFORMATION

Additional supporting information may be found in the online version of the article at the publisher's website. [Correction added on March 01, 2022, after first online publication: Revised supporting information has been updated.]

How to cite this article: Degro, C. E., Bolduan, F., Vida, I., & Booker, S. A. (2022). Interneuron diversity in the rat dentate gyrus: An unbiased in vitro classification. *Hippocampus*, *32*(4), 310–331. https://doi.org/10.1002/hipo.23408